Diffusion MRI of Cancer: from Low to High b-Values

Lei Tang, M.D.[1] and **Xiaohong Joe Zhou, Ph.D.**[2,*]

[1]Department of Radiology, Peking University Cancer Hospital & Institute, Key laboratory of Carcinogenesis and Translational Research, Beijing, China

[2]Center for MR Research and Departments of Radiology, Neurosurgery, and Bioengineering, University of Illinois at Chicago, Chicago, IL, USA

Abstract

Following its success in early detection of cerebral ischemia, diffusion-weighted imaging (DWI) has been increasingly used in cancer diagnosis and treatment evaluation. These applications are propelled by the rapid development of novel diffusion models to extract biologically valuable information from diffusion-weighted MR signals, and significant advance in MR hardware that has enabled image acquisition with high b-values. This article reviews recent technical developments and clinical applications in cancer imaging using DWI, with a special emphasis on high b-value diffusion models. The article is organized in four sections. First, we provide an overview of diffusion models that are relevant to cancer imaging. The model parameters are discussed in relation to three tissue properties – cellularly, vascularity, and microstructures. An emphasis is placed on characterization of microstructural heterogeneity, given its novelty and close relevance to cancer. Second, we illustrate diffusion MR clinical applications in each of the following three categories: (a) cancer detection and diagnosis; (b) cancer grading, staging, and classification; and (c) cancer treatment response prediction and evaluation. Third, we discuss several practical issues, including selection of image acquisition parameters, reproducibility and reliability, motion management, image distortion, etc., that are commonly encountered when applying DWI to cancer in clinical settings. Lastly, we highlight a few ongoing challenges and provide some possible future directions, particularly in the area of establishing standards via well-organized multi-center clinical trials to accelerate clinical translation of advanced DWI techniques to improving cancer care on a large scale.

Keywords

Introduction

Diffusion-weighted imaging (DWI) was introduced to MRI in the mid-1980s[1]. Following its immense success in early detection of cerebral ischemia[2,3], which has significantly impacted

---

[*]**Corresponding Author Info:** X. Joe Zhou, PhD, MRI Center, MC-707, Suite 1A, 1801 West Taylor Street, University of Illinois at Chicago, Chicago, Illinois 60612, USA., xjzhou@uic.edu; Phone: +1 312-413-3979; Fax: +1 312-355-1637.

stroke patient management, considerable efforts in DWI have been directed towards cancer[4]. Over the past two decades, such efforts have been accelerating. This is largely stimulated by the promise that DWI can probe tissue cellularity, microstructures, and microvasculature at a sub-voxel level, all of which are of great importance to cancer. The exciting DWI applications to cancer are enabled by the rapid development of novel diffusion models[5] to extract biologically valuable information from diffusion-weighted MR signals, and significant advances in MRI hardware[6] and image acquisition technologies to facilitate translation of advanced DWI techniques to clinical practice.

Undoubtedly, DWI for cancer applications has benefited immensely from the rich experience gained from stroke imaging. However, applying DWI to cancer is not a simple extension of prior success with ischemic stroke. First, cancer is a disease with a much broader scope than stroke, affecting many organ systems beyond the brain. As such, new diffusion imaging strategies must be developed and a number of new challenges, such as respiratory motion and drastic magnetic susceptibility variations in the body, must be addressed. Second, compared to cerebral ischemia, cancer is a more complex disease that involves many biological processes spanning from genetics, metabolism, microenvironment, microstructures, to angiogenesis. This complexity presents new challenges for DWI to probe some of these biological processes. Third, DWI of cancer places a stronger emphasis on quantitative markers with biological significance. Hence, developing various diffusion models and understanding the associated model parameters become critical. Lastly, applications of DWI to cancer are not limited to detection and diagnosis, but extend into areas such as cancer staging, grading, treatment evaluation, and even prediction.

The differences outlined above represent enormous opportunities for developing advanced DWI techniques with a focus on cancer applications. Up to date, DWI for the vast majority of cancer applications has been relying on the simplest diffusion model based on mono-exponential signal decay that yields a single diffusion parameter – the apparent diffusion coefficient (ADC). Despite its simplicity, this mono-exponential model has worked remarkably well in a broad range of cancer applications. Many studies have provided compelling evidence relating ADC to tissue *cellularity*[7,8], an important cellular measure during cancer progression and treatment-induced regression. More recently, using an established model based on intravoxel incoherent motion (IVIM)[9,10], an increasing number of studies have suggested that measurement of the "fast diffusion" component in tissues can be related to perfusion, providing an indirect measure of tissue *vascularity*[11] and the associated tumor angiogenesis. Very recently, with the development of a wealth of advanced diffusion models, diffusion MRI has been shown capable of probing tissue *microstructures* at a sub-voxel level[5]. Although the majority of tissue microstructural studies are performed on the brain, applications to the non-CNS systems have emerged, including but not limited to prostate cancer[12], breast cancer[13], and gastrointestinal stromal tumor (GIST)[14]. In this review, we will focus on the three aforementioned aspects – cellularity, vascularity, and microstructures – that diffusion MRI can offer for cancer detection, characterization, and therapy evaluation. A special emphasis will be placed on microstructural characterization at high b-values, given its novelty and lack of systematic review in this rapidly growing area with immense potential.

This review is organized in four sections. First, we will provide an overview of diffusion models that are particularly relevant to cancer imaging. The model parameters will be discussed in relation to the three tissue properties – cellularly, vascularity, and microstructures. Second, we will review selected diffusion MRI clinical applications in each of the following three areas: (a) cancer detection and diagnosis; (b) cancer grading, staging, and classification; and (c) cancer treatment evaluation and prediction. We recognize that organ-specific cancer types have varying pathological characteristics and clinical context, leading to differences in the use and interpretation of DWI. As such, the review of the clinical literature will focus on illustration of general principles without delving into the specific cancer types. In addition, pre-clinical studies using animal models will not be covered in our review. Third, we will discuss several practical issues, including selection of image acquisition parameters, reproducibility and reliability, motion management, image distortion, etc., that are commonly encountered when applying DWI to cancer in clinical settings. Lastly, we will highlight a few ongoing challenges and provide some possible future directions.

1.   Diffusion Models and Their Biophysical Bases

1.1   Diffusion-Weighted MR Signals

It is well known that the MRI signal is attenuated by diffusion. For water diffusion in a homogeneous medium where the diffusion displacement follows a Gaussian distribution (e.g., in the cerebrospinal fluid), a simple mono-exponential decay function can well describe the diffusion-induced signal attenuation S:

$$S = S_0 \exp(-bD), \quad [1]$$

where D is the diffusion coefficient, S_0 is the signal in the absence of diffusion, and b is known as b-value which determines the degree of diffusion weighting in the signal. Although Eq. [1] is extensively referenced in the literature, it is rarely valid in biological tissues because heterogeneous cellular and sub-cellular microstructures can substantially perturb the Gaussian distribution of diffusion displacement, leading to non-Gaussian diffusion. This non-Gaussianity provides us with a valuable window through which tissue cellularity, vascularity, microstructures, and heterogeneity can be visualized.

1.2   b-Value "Spectrum"

The b-value in Eq. [1], a critical parameter in DWI, not only controls the degree of diffusion-weighting in the image, but also encodes different tissue properties into the DWI signals. Irrespective of the degree of deviation from Gaussian diffusion, MR signals always decrease as b-value increases (Figure 1). The rate of signal decrease, however, depends on the b-values. At a relatively low b-value (e.g., b < 200 s/mm^2), the signal decays rapidly because fast water movement in capillary vessels can cause substantial signal loss in addition to diffusion-induced signal attenuation. This effect makes the low b-value region particularly sensitive to tissue vascularity, as further described below in the IVIM model. As b-value increases, signal loss from the capillary vasculature is complete, making the

diffusion process a dominant contributor to the signal attenuation. In this intermediate b-value range (e.g., 500 – 1500 s/mm^2), the signal attenuation is sensitive to spatial scale of a cellular size and hence strongly correlates to cellularity as illustrated in Figure 1. When the b-value increases further, the signal attenuation enters the "high b-value" regime where the sensitivity to smaller spatial scale increases, making diffusion MRI suitable for probing tissue microstructural complexity and heterogeneity. A consensus for a high b-value threshold has not been established in the literature. Typically, high b-value refers to b>2000 s/mm^2 for neuro applications and >1000 s/mm^2 for body applications. The varying signal attenuation behavior as a function of b-value is analogous to a spectrum where information content depends on frequency. Hence, the schematic diagram shown in Figure 1 can be referred to as a "b-value spectrum" to facilitate discussion within the scope of this review.

1.3   Mono-exponential Model and Cellularity

Mono-exponential diffusion model is the original model that remains to be the most prevalent for cancer imaging applications. Given the relatively low spatial resolution in DWI (e.g., 2–5 mm in a linear dimension of a voxel), the intra-voxel structural variability and heterogeneity can be substantial. Despite this structural complexity, the mono-exponential model uses a single diffusion coefficient – ADC – to approximate the *average* diffusion process within a voxel. The mathematical expression can be derived by replacing D in Eq. [1] with ADC which can be measured by acquiring two images with different b-values[4].

It was observed that DWI signal in biological tissues decays bi-exponentially as shown in Eq [2a][15], particularly at high b-values (e.g., > 1500 s/mm^2 for brain tissues). One of the explanations is that the faster diffusion coefficient (D_f) is associated with the diffusion process in the extra-cellular space, whereas the slower one (D_s) in the intra-cellular space because of increased restrictions caused by sub-cellular structures (Figure 2). The voxel-based ADC, therefore, represents the volume-weighted average of the fast and slow diffusion coefficients shown in Eq. [2b]:

$$S = S_0\left[V_f\exp\left(-bD_f\right) + V_s\exp\left(-bD_s\right)\right] \quad [2a]$$

$$ADC = \frac{V_f D_f + V_s D_s}{V_f + V_s}, \quad [2b]$$

where V_f and V_s are the volume fractions of the fast and slow diffusion component, respectively. Equation [2b] is important because it links ADC to cell volume fraction or cellularity of a voxel, provided that V_f and V_s correspond to extra- and intra-cellular volumes, respectively. Although such correspondence has been challenged by several experimental observations which indicate that cell membrane likely plays an important role in diffusion compartmentalization[16], a large number of studies on many types of cancer have indicated strongly that ADC is negatively correlated with cell density or cellularity (average

correlation coefficient $r = -0.61$)[7,17]. These studies have established ADC as a quantitative surrogate for tissue cellularity.

1.4   IVIM Model and Vascularity

In addition to the intra- and extra-cellular spaces, microvasculature can also be a significant component in an image voxel (Figure 2), particularly in cancerous tissues due to angiogenesis. By including the vascular contribution to the signal, the IVIM model extends the mono-exponential diffusion model into the following form[9,10]:

$$S = S_0[f\exp(-bD^*) + (1 - f)\exp(-bD)], \quad [3]$$

where f is the volume fraction of the vasculature in a voxel and D^* is a pseudo-diffusion coefficient that corresponds to water movement in the microvasculature, or the perfusion process. The first term in Eq. [3] represents the vascular contribution, whereas the second term accounts for the diffusion contribution. To capture both contributions, a minimum of three b-values are requires, for example, b = 0, 50, and 800 s/mm^2, as typically used for liver imaging. Since water movement in perfusion is much faster than that in diffusion, a relatively small b-value (50–200 s/mm^2) is used to sensitize perfusion without causing excessive signal attenuation. The corresponding D^* can be obtained by using the two lower b-value images (e.g., b = 0 and 50 s/mm^2), while ADC can be calculated from the higher b-value images (e.g., b = 50 and 800 s/mm^2).

Either f or D^* can be used to approximate tissue perfusion. The combinations of these two parameters (fD^*) has also been used for improved performance[11,18]. It should be noted that the IVIM model provides only an approximation of tissue perfusion. As such, D^* or f may not replace tissue perfusion measurement. Nonetheless, the IVIM model described by Eq. [3] offers a means to access to tissue vascularity via a simple diffusion measurement. The reproducibility and reliability of the measurement on tissue vascularity can be substantially improved by increasing the number of b-values (e.g., 6) in the range of 0–200 s/mm^2 [19].

1.5   Non-Gaussian Models and Microstructures

Although non-Gaussian diffusion behaviors exist irrespective of b-value, they become most evident at high b-values, e.g., > 2000 s/mm^2. A large number of non-Gaussian diffusion models have been developed with a common goal to relate diffusion model parameters to biologically relevant tissue microstructures at the sub-voxel level. The non-Gaussian diffusion models can be classified into two categories: compartmentalized and non-compartmentalized models.

Compartmentalized models divide each voxel into multiple compartments based on tissue structural or diffusion properties. Examples of compartmentalized models include bi-exponential model (Eq. [2a][15], AxCaliber[20], NODDI (neurite orientation dispersion and density imaging)[21], CHARMED (composite hindered and restricted model of diffusion)[22], VERDICT (vascular, extracellular, and restricted diffusion for cytometry in tumors)[12], RSI (restriction spectrum imaging)[23], etc. The vast majority of these models have been

developed for the brain without a specific focus on cancer imaging. One of these models – VERDICT, however, has been developed for cancer applications and successfully applied to colorectal and prostate cancers[12]. VERDICT divides each voxel into three compartments to capture the main tumorous tissue features that influence the DWI signal. These three compartments include (a) water trapped in cells, (b) water in the vascular network, and (c) interstitial water. The signal in DWI can, therefore, be expressed as the summation of these three compartments: $S = \sum_{i=1}^{3} f_i S_i$, where f_i is the volume fraction of each compartment whose signal intensity is S_i. Unlike the mono-exponential or IVIM model, VERDICT provides estimates of specific tissue properties such as the size and packing density of the cells, as well as the vascular and extracellular-extravascular volume fractions.

Another compartmentalized model is RSI initially developed for the brain[23], but recently extended to the prostate[24]. In RSI, the diffusion signal is modeled as a mixture of up to eight components with varying degrees of diffusion restriction or hinderance. Each component describes the signal dependence on a specific tissue property (e.g., cell size, density, orientation, etc.). The overall signal thus becomes the weighted sum of these components. By determining the individual weights using a generalized linear estimation technique, the underlying tissue parameters (e.g., size and shape/orientation of hindered and restricted water compartments) can be obtained.

Unlike the compartmentalized models, non-compartmentalized models do not assume a specific number of tissue compartments. Instead, the possible tissue compartmentalization is embedded in the model parameters such as diffusion heterogeneity index, distributions of diffusion coefficients, or kurtosis. Examples of non-compartmentalized models include diffusion kurtosis imaging (DKI)[25], stretched exponential model[26], fractional order calculus (FROC) model[27], continuous-time random walk (CTRW) model[28,29], fractional motion (FM) models[30,31], etc. Among these models, diffusion kurtosis imaging (DKI) has been used extensively in cancer imaging.

The diffusion kurtosis model, expressed in Eq. [4], generalizes the mono-exponential Gaussian model to the non-Gaussian regime. It offers two parameters: diffusion coefficient (similar to ADC) and dimensionless kurtosis K which describes the deviation of water molecular displacement from a Gaussian distribution.

$$S = S_0 exp\left[-bD + \frac{1}{6}K(bD)^2\right]. \quad [4]$$

Mathematically, the kurtosis model incorporates a second-order term to account for deviations from Gaussian diffusion behavior. Its biophysical basis has been discussed in a number of recent studies aimed at establishing a link between K and specific aspects of tissue microstructures[32–34]. It is worth noting that the DKI model has been more commonly used to study diffusion anisotropy as an extension of diffusion tensor imaging (DTI), which involves image acquisitions with multiple b-values *and* multiple diffusion gradient directions. For clinical applications in cancer imaging where the imaging times are an

important consideration, DKI can be used by acquiring trace-weighted images to save time and remove the sensitivity to diffusion anisotropy[3].

Another non-compartmentalized model is the stretched exponential model (Eq. [5]) where diffusion non-Gaussianity is accounted for by introducing an empirical parameter a. In this model, the diffusion coefficient D is referred to as distributed diffusion coefficient (DDC) because a single diffusion coefficient is no longer sufficient to describe diffusion process in a complex and heterogeneous tissue.

$$S = S_0 \exp\left[(-bD)^{\alpha}\right]. \quad [5]$$

The empirical nature of the stretched exponential model was mitigated by the development of the FROC and CTRW models[27–29,35]. Both models recognize the presence of intra-voxel diffusion heterogeneity in *space* and *time*. Water molecules can produce a variable spatial displacement in each move (i.e., spatial heterogeneity), or can take a variable temporal interval to make a move (i.e., temporal heterogeneity). The spatial heterogeneity is a direct reflection of the underlying tissue structural complexity, while the temporal heterogeneity reflects the likelihood of the water molecule to be "trapped" or "released" while it diffuses through the complex tissue structures. Hence, both spatial and temporal diffusion heterogeneities originate from the underlying tissue structural heterogeneity. In the CTRW model, the temporal and spatial diffusion heterogeneities are described by two model parameters, α and β, respectively:

$$S = S_0 \quad E_{\alpha}\left[-(bD)^{\beta}\right], \quad [6]$$

where E_{α} is a Mittag-Leffler function[28,29] of the α order, β corresponds to spatial diffusion heterogeneity, and both α and β are bounded in the range of 0 and 1. In a homogeneous medium, both α and β are equal to 1 and Eq [6] reduces to the monoexponential decay function in Eq. [1][29]. As the degree of tissue heterogeneity increases, these parameters become progressively less than 1.

The FROC model is a simplification of the CTRW model by considering the spatial heterogeneity only (i.e., assigning α =1). For a Stejskal-Tanner diffusion gradient G_d with a duration δ and gradient separation $\otimes$, the diffusion-induced signal loss is expressed as[27]:

$$S = S_0 \exp\left[-D\mu^{2(\beta-1)}(\gamma G_d\delta)^{2\beta}\left(\Delta - \frac{2\beta-1}{2\beta+1}\delta\right)\right], \quad [7]$$

where μ is a spatial constant to preserve the nominal units of diffusion coefficient D in mm^2/s. Both CTRW and FROC models have been increasingly used for cancer imaging, as detailed later. To use either model, a relatively high b-value (e.g., ≥3000 s/mm^2) is required.

To apply high b-value DWI to studying tissue microstructures, it is important to recognize that the ability of probing tissue microstructures depends heavily on the diffusion time – a parameter which is typically fixed on commercial MRI scanners. The diffusion time controls the spatial scale of the tissue structures under investigation[36]. For a spin echo sequence, the shortest diffusion time is determined by the available gradient strength, while the longest by the maximal TE to retain a minimally required signal-to-noise ratio (SNR). These limits can be overcome by using alternative pulse sequences[36].

In addition to the specific diffusion models outlined above, other diffusion models have also been used for cancer imaging. Table 1 summarizes a set of selected diffusion models, the key model parameters, the typical b-value ranges, and the biological significance of these models in relation to cancer-relevant tissue properties.

2.   Clinical Applications

2.1   Detection and Diagnosis

Despite its relatively low spatial resolution, DWI plays an important role in cancer detection because it can offer advantages in tumor-to-normal tissue contrast. Because water diffusion in highly cellular tumor is more restricted than in the normal tissues, a higher b-value can more effectively suppress signals from the normal tissue, enhancing tumor-to-normal tissue contrast and leading to hyperintense signals in the tumor (Figure 3). Such enhanced contrast can considerably improve the conspicuity of small lesions (Figure 4)[37], tumors on hollow organs[38], and tumors obscured by strong background from normal tissues[39].

While the majority of the reported studies have used a low to moderate b-values (e.g., ~800 s/mm^2 for the liver, and 1000 s/mm^2 for the brain) because of the SNR considerations, the benefits of using a higher b-value beyond the conventional have been increasingly demonstrated in recent studies. Ichikawa et al. employed a b-value of 1000 s/mm^2 to detect colorectal adenocarcinoma in a cohort of 33 patients with colonoscopically proven colorectal cancers[40]. They achieved a high sensitivity of ~90% and a specificity of ~100%. Over the years, the threshold for high b-value is evolving. Kim et al.[41] compared the performance between b-values of 1000 and 2000 s/mm^2 for detection of prostate cancer at 3 Tesla and concluded that DWI performed using a b-value of 1,000 s/mm^2 was more sensitive and more accurate in predicting localized prostate cancer than b-value of 2,000 s/mm^2. However, Wetter et al. reported that the contrast ratios of diffusion-weighted images were significantly higher at b-values of 1500 and 2000 s/mm^2 in comparison to b-values of 800 and 1000 s/mm^2, illustrating the benefits of high b-values for detecting prostate cancer[42]. The potential value of high b-values for cancer detection has also been investigated in several other cancers[43,44]. Despite some conflicting reports, the general consensus is that higher b-values can provide better conspicuity for tumor detection, provided that an adequate SNR (e.g., 5–10) can be maintained[45,46]. This has led to recent adoption of high b-value (1400–2000 s/mm^2) DWI in Prostate Imaging Reporting and Data System (PI-RADS) Version 2[47]. Achieving an adequate SNR at high b-values can be challenging. A possible solution is to synthesize high b-value images from acquired low b-value images (which have high SNR) using a specific diffusion model – commonly a mono-exponential model. As

such, the synthetic images cannot be used with advanced diffusion models other than the model from which they are synthesized.

The use of quantitative information from DWI can further aid in differential diagnosis of tumors. Because the effect of non-Gaussian diffusion increases with the b-value, it is widely reported that the ADC value depends on b-value selections, particularly in the high b-value range (e.g., b> 1000 s/mm^2)[48].

With the ability to offer multiple parameters, non-Gaussian diffusion models can be helpful in cancer characterization and/or detection. For example, diffusion parameter maps can be used individually or conjointly to create or enhance the tumor-to- tissue contrast. Figure 5 illustrates how the individual α, β and D maps from a CTRW model are used to highlight a high-grade medulloblastoma in an 18-month old girl. The multiparametric contrasts provide complementary information to conventional T1-, T2-, and FLAIR contrasts, improving cancer detection and/or characterization. Using a DKI model with 11 b-values up to 1500 s/mm^2, Tamura et al. have observed the differences in DKI parameters between prostate cancer, benign prostatic hyperplasia (BPH), and benign peripheral zone (PZ)[32]. In particular, K is significantly higher in prostate cancer than in nonstromal BPH and healthy PZ. Other non-Gaussian models, such as stretched exponential[49,50], VERDICT[12], and RSI[24], have also been successfully used for prostate cancer detection. Although the majority of the studies have demonstrated the advantages of non-Gaussian models with high b-values, one study has shown that the DDC ratio between the breast cancer and glandular tissue, estimated from a stretched exponential model, did not show significant differences from the ADC ratio[51]. In addition, another study did not find that the FROC model parameters outperformed ADC for differentiating between malignant and benign breast lesions, likely because of the intrinsic high degrees of heterogeneity within the breast tissue and/or a moderate maximal b-value employed in the study[13].

At the other end of the b-value spectrum, the IVIM model has been increasingly applied to cancer diagnosis and detection, as reviewed by Koh et al.[11] Improved performance of IVIM parameters (D^*, D, and f) over ADC has been reported for diagnosing focal liver lesions[52], and differentiating between benign and malignant breast lesions[53]. The IVIM model has also been shown useful in discriminating lung cancer from obstructive pulmonary consolidation[39]. Very recently, Qi et al. showed that the combination of two IVIM parameters. f and D, can improve differentiation of malignant versus benign mediastinal lymph nodes[19], which is of great value for determining lymph node involvement in lung cancer and other neoplasms.

In addition to detecting primary tumors, DWI with high b-values has also been used to facilitate the detection and diagnosis of residual or recurrent tumors after surgical or non-surgical local treatments (stereotactic body radiation therapy or SBRT, transcatheter arterial chemoembolization, radiofrequency ablation or RFA, stereotactic radiotherapy/radiosurgery or SRT/SRS, etc.) and palliative therapy[54,55]. Figure 6 shows images from an HCC patient who received RFA. No obvious enhancement was seen near the post-RFA area in the T1-weighted image (Figure 6a). However, recurrent lesions were detected as dot-like high

signals in DWI (Figure 6c). These lesions progressed rapidly after another month (Figures 6b and 6d).

2.2   Classification, Grading, and Staging

Recent initiatives in predictive, personalized, preemptive, and participatory medicine are shifting the roles of radiology from conventional diagnosis to disease classification, grading, staging, and prognostic assessments[56]. Oncologists are increasingly expecting radiologists to provide pretherapy information, such as tumor classification and grading, to guide their treatment plans in order to achieve an optimal outcome for cancer patients. Unfortunately, conventional MRI based on morphological features is inadequate to meet this challenge. With its sensitivity to tissue microstructures at a sub-voxel level, high b-value DWI can contribute immensely to addressing this unmet need.

Intra-tumoral heterogeneity is an important consideration in glioma grading[57], breast cancer staging[58], Gleason scoring for prostate cancer[59], and predicting biological aggressiveness of premalignant esophageal lesions[60]. Previous imaging studies on intra-tumoral heterogeneity were limited by the achievable voxel size. The advent of high b-value DWI has shown great potential in breaking this barrier and peeking into the voxels. Using a stretched exponential model with a maximal b-value of 4000 s/mm^2, Kwee et al. observed a substantially lower α value in high-grade gliomas than in the normal brain tissues and attributed this difference to elevated intra-voxel heterogeneity in the tumor[61]. The intra-voxel heterogeneity was more rigorously investigated by relating tissue structural heterogeneity to spatiotemporal diffusion heterogeneities in the FROC and CTRW models[27–29,62]. Using a FROC model with a maximal b-value of 4000 s/mm^2, Sui et al. observed a significant difference in β (i.e., intra-voxel diffusion spatial heterogeneity) not only between pediatric brain tumors and normal brain tissues, but also between low-grade and high-grade tumors[62]. The combination of β and D from the FROC model produced a diagnostic accuracy of 92.5% for differentiating low- and high-grade pediatric brain tumors, considerably outperforming that of ADC (accuracy = 80.6%). Similar results were also obtained for differentiating low- and high-grade gliomas in adults using a FROC model[63] (Figure 7), and for differentiating low- and high-grade brain tumors in children using a CTRW model where both spatial and temporal diffusion heterogeneities are considered[29]. Diffusion-based tumor heterogeneity studies are not limited to the brain tumors and has been extended to breast cancer[13], prostate cancer[64], gastric cancer[14], and others. In addition, diffusion-based tumor heterogeneity studies are not limited to the aforementioned models. For example, by investigating diffusional variance caused by microscopic anisotropy and isotropic heterogeneity, Szczepankiewicz et al. demonstrated that a high b-value DWI technique, known as density by diffusional variance decomposition (DIVIDE), is also sensitive to brain tumor heterogeneity[65].

Other aspects of tissue microstructures can also be probed through non-Gaussian diffusion parameters for tumor characterization. Zhu et al. found kurtosis derived from DKI demonstrated a stronger correlation with histologic grades and T staging of rectal cancer compared with ADC[33]. Wen et al. applied NODDI to characterize gliomas at 7 Tesla[66]. Significant differences in NODDI parameters were observed between the tumor and normal appearing white matter. However, no significant differences were found across different

glioma grades[66]. Bai et al.[34] compared the performance for glioma grading using mono-exponential, bi-exponential, stretched exponential, and DKI models with b-value up to 5000 s/mm^2. Their results indicate that a in the stretched exponential model and mean K in the DKI model outperformed the conventional diffusion parameters such as ADC for glioma grading. The optimal parameters for tumor grading depend strongly on specific tumors. In another study on differentiating types I and II epithelial ovarian cancer (EOC) using high b-value DWI with mono-exponential, bi-exponential and stretched exponential diffusion models[67], ADC, D from the IVIM model, and DDC are all adequate for EOC differentiation, but there is no significant difference among these parameters. Yet another study by Roethke et al. reported no significant benefit of DKI for detecting and grading of prostate cancer as compared with ADC in the peripheral zone[68]. In all the studies outlined above, a common challenge is that *physical* or *mathematical* parameters from various diffusion models are attempted to improve tumor grading, staging, and characterization. The direct relationship between these parameters to intravoxel tissue microstructures has not been fully established or validated. In addition, the accuracies in some high b-value DWI studies may not be as high as those of conventional MRI. However, DWI can be combined with conventional sequences to improve the overall accuracy, as recently demonstrated by Chatterjee et al. in a technique known as hybrid multidimensional MRI[69]. Assessing the biological aggressiveness of tumors is another important aspect for cancer patient evaluation and management. With its correlation to cellularity, ADC can be an important marker for biological aggressiveness of tumors, as in the assessment of the NIH risk stratification of gastrointestinal stromal tumors (GIST)[70]. It is generally believed that the lower the ADC, the higher degree of malignancy and the poorer prognosis. Exceptions, however, do exist. Lee et al. reported that ADC of the mass-forming intrahepatic cholangiocarcinoma with poor prognosis was higher[71], because of abundant fibrous stroma with scanty tumor cellularity. A similar exception can be found in mucinous cancer of gastrointestinal (GI) tract, which has poorer prognosis but higher ADC because of a large amount of the mucinous lake[72]. Exceptions can also be found in some primary brain tumors that have higher ADC than the surrounding tissue, likely due to the vasogenic edema associated with the tumor, which results in a relatively less net increase (or even decrease) in cellularity within a highly cellular brain tissue.

2.3 Evaluation and Prediction of Treatment Response

Over the recent years, a number of novel cancer treatment regimens have emerged. Neoadjuvant chemotherapy (NACT) has become the standard procedure for many advanced malignant tumors before surgery. Targeted therapy and PD-1/PDL-1 immunotherapy are emerging as an effective alternate to traditional chemotherapy, and have become even the first-line treatment under some situations[73,74]. Precise radiotherapy, as well as other non-surgical local treatments (SBRT, TACE, IRA, SRS/SRT, etc.), has prompted cancer treatment to the era of minimal invasiveness. As the treatment options expand, early evaluation, or even prediction, of the treatment efficacy becomes increasingly crucial. Traditional response evaluation based on size or morphologic changes, as stipulated in the RECIST criteria, can no longer meet the need for personalized patient care[75]. This represents an excellent opportunity for DWI to become an additional surrogate to complement RECIST or other criteria such as RANO[76]. Together, they have great potential

to address the unmet need for treatment assessment and overcome the limitations of the existing criteria.

DWI for prediction of treatment response and prognosis—As for prediction, it is generally believed that the lower the pre-treatment ADC, the better of treatment responses[77–80]. A lower pre-treatment ADC typically indicates more active tumor parenchyma which supports a larger amount of blood supply (as opposed to necrotic tissues, for example) to facilitate easier transportation of anticancer agents to the targeted tumors[77]. Conversely, tumors with higher pre-treatment ADC can be hypoxic with a slower metabolism, making them insensitive to radiotherapies[81]. For other treatment methods, however, the results can be reversed. For example, Mannelli et al. found that HCCs with poor response to TACE had significantly lower pre-treatment ADC compared to HCCs with good response[82]. Very recently, IVIM model has also been applied to predicting response to neoadjuvant treatment of breast cancer[83]. It was reported that $D*$ showed prognostic capabilities, whereas baseline ADC and D were not significant predictors of response.

DWI for assessment of early response—A major unmet need is whether treatment evaluation can be obtained earlier than what RECIST criteria can presently offer, i.e., 2–3 months after the initiation of treatment. Some tumors may change rapidly in cellularity, vascularity, microstructures and heterogeneity in response to targeted agents, but these changes may not result in tumor size change that can be detected morphologically by CT or MRI. The sensitivity to cellularity, vascularity, microstructures and heterogeneity makes DWI an ideal candidate to capture these changes early.

DWI for early treatment evaluation was initially illustrated in brain tumors using ADC[4,84,85]. Moffat et al. showed that substantial ADC change can be observed 3 weeks during a 6-week course of radiation therapy[84]. This success was extended to a large number of studies where ADC was used for early evaluation of chemotherapy, targeted therapy, and immunothepary[4,77]. In many these studies, ADC change was observed as early as 1–2 weeks after the initiation of treatment[77,86]. Tang et al. have reported a marked ADC increase (44.8%) at 1 week after therapy which was associated with good response to imatinib mesylate in patients with GIST[77]. Figure 8 demonstrates a case of GIST which had distinct changes of ADCs just after three days of imatinib targeted therapy. The change in ADC continued for four weeks in the follow-up scans.

High b-values with or without non-Gaussian models have been used for early evaluation of cancer treatment. Using a Gaussian model with b-values up to 4000 s/mm^2, Mardor et al. reported that pre-treatment ADC and a diffusion index $R(D)$ can both correlation well ($r = 0.76$–0.77) with brain tumor response to radiation therapy[87]. The strong correlation implies that tumors with low pretreatment diffusion values will respond better to radiotherapy than those with high diffusion values. Over the past few years, an increasing number of non-Gaussian models have been applied to cancer treatment evaluation. McDonald et al. recently demonstrated that RSI with high b-values can be more immune to confounding factors such as edema and offers advantage over ADC in evaluating response of high-grade gliomas to bevacizumab[88]. This is an interesting example of how higher order DWI modeling can be useful when the primary effect of bevacizumab therapy is on edema and not tumor

cellularity. Using a FROC model with a combination of the pre-treatment β value and post-treatment change of ADC at 2 weeks, Tang et al. demonstrated that GIST response to sunitinib second-line targeted therapy can be assessed at early as 2 weeks after the initiation of therapy[14]. Figure 9 shows an example illustrating the sensitivity of β from the FROC model to sunitinib targeted therapy. Parameters from Gaussian and non-Gaussian diffusion models can be also combined across a broad b-value range to improve the performance of response to chemotherapy, as recently demonstrated by Zhu et al., for locally advanced rectal cancer[89].

DWI was also useful for evaluating response of non-surgical local treatment, such as irreversible electroporation (IRE) of pancreatic carcinoma[90] and stereotactic body radiotherapy (SBRT) of lung cancer[91]. Kokabi et al. reported that ADC change 3 hours after TACE treatment could predict the response of unresectable HCC to doxorubicin drug-eluting beads transcatheter arterial chemoembolization (DEB-TACE)[92]. Attention should be paid to other pathologic changes, such as gelatinous necrosis and small abscess in tumor after treatment (especially after anti-angiogenic targeted therapy for brain tumor[93]) that may display high signal on DWI, mimicking recurrent (Figure 10). Thus, DWI must be used in combination with conventional images to avoid misinterpretation.

DWI as a supplement to RECIST criteria at regular evaluation time points—
Besides prediction and early evaluation, DWI can be also helpful at conventional evaluation time-points, i.e., 2–3 months after therapy, to complement the widely used RECIST criteria. The existing RECIST criteria have at least two limitations. First, RECIST is not suitable for evluating GI tract tumors because the variable shape of the GI wall precludes reliable measurement of the long lesion dimension. As such, RECIST defines the primary lesions of GI tract as non-targeted lesions, resulting in a dilemma for NACT evaluation. ADC and its non-Gaussian counterparts can provide quantitative indicators to help resolving this dilemma, as demonstrated in a rectal cancer study to evaluate response to chemoradiation therapy[94] and a gastric cancer study to evaluate chemotherapy[95]. In addition, DWI also serves as an sensitive indicator for complete response of rectal cancer or to help clinical evaluation for patients under "wait-and-see" surveillance[96].

Second, new palliative treatment agents such as targeted therapy and immunotherapy may cause the tumor size to increase but with tissue degenerations (e.g., cystic degeneration, necrosis, hemorrhage, and mucinous degeneration). Some of these tissue changes can be measured by DWI, as reported in the GIST response to imatinib and sunitinib treatments[14,77], HCC to sorafenib treatment[97], and lung cancer to antivascular targeted therapy[98].

3. Practical Considerations

3.1 Selection of b-Values

Selection of b-values is one of the most important tasks in DWI, requiring a number of considerations. First, proper b-value selection is strongly coupled with the diffusion model to be used for image analysis. The typical range of b-values for some selected diffusion models is listed in Table 1. For example, when using the IVIM model, 6 b-values in the

range of 0–200 s/ mm^2 are recommended to ensure reliability and reproducibility in extracting the IVIM parameters. When using the CTRW or FROC model, the upper bound of the b-values should typically exceed 3000 s/mm^2. Second, the selection of b-values depends on the organ under study. For brain imaging, a nominal b-value of 1000 s/mm^2 is often chosen for ADC calculations because the average diffusion coefficient of brain tissue is ~1×10^{-3} mm^2/s, producing an average diffusion attenuation of e^{-1}. For tissues in organs with a slower average diffusion coefficient, a higher b-value should be selected, and vice versa. Third, the SNR and diffusion contrast should be simultaneously considered. Although a higher b-value produces a better diffusion contrast, the SNR can be substantially reduced due to the increased diffusion-induced signal loss as well as T2-induced signal attenuation caused by a longer TE to support the higher b-value. The optimal balance between the SNR and image contrast is typically determined empirically. Lastly, a high b-value requires a strong diffusion gradient to be activated for a long time, which may exacerbate artifacts related to gradient-induced vibration and/or eddy currents.

3.2 Repeatability and Reliability of Diffusion Models

Repeatability and reliability are important for quantitative DWI applications, particularly in determining a diagnostic threshold. Several studies have reported good reliability or repeatability for ADC, slow D in IVIM, and stretched exponential parameters, whose coefficients of variance (CV) are within 20%[99–102], but worse for f and $D*$ in the IVIM model (30%−80%) in studies on lung cancer[99], HCC[100], and ovarian tumors[101]. A study on pediatric patients reported that parameters based on IVIM or DKI models had worse CV than those from the stretched exponential model[102]. Reproducibility on other high b-values model parameters has not been adequately reported in the literature. When advanced diffusion models are used, a higher b-value and/or larger number of diffusion gradient directions increases the vulnerability to noise and/or motion, which can compromise the reliability and reproducibility. A comprehensive understanding of reliability and reproducibility is needed to accomplish full clinical translation of advanced DWI techniques.

3.3 Motion Management during DWI

DWI is particularly sensitive to motion during image acquisition. The use of echo planner imaging (EPI) and other motion resilient pulse sequences such as PROPELLER can effectively avoid or manage the inter-shot motion within acquisition of an image. However, inter-image motion (e.g., for different b-values) must also be addressed, particularly for body imaging. Several methods have been used to control motion for body DWI, such as breath-hold to freeze respiratory motion, respiratory triggering to synchronize with breathing, hypotonic agents to control peristalsis, and echocardiography triggeringto eliminate the influence of heartbeat. Selection of a proper motion management strategy is highly application dependent.

Chen et al. compared four motion management techniques: multiple breath-hold (MBH), free-breathing (FB), respiratory-triggered (RT), and navigator-triggered (NT) diffusion imaging on the liver, and recommended FB because of its superior reproducibility and shorter acquisition times[103]. Studies reported by Bernardin et al.[104] and Weller et al.[105] are also in favor of FB for DWI of the lung because it provides good intra- and inter-observer

repeatability in ADC measurements for malignant lung tumors. A general consensus, however, has not been reached. For example, for DWI of the liver, Kim et al. recommended BH[106], whereas Lee et al. showed advantages of using echocardiography triggering which was more effective for decreasing regional variability of ADC and IVIM parameters than FB or RT and improved measurement repeatability by reducing cardiac motion-induced errors[107].

In the literature, there appears to be a stronger preference to FB when using a single-shot EPI-based diffusion sequence. With this approach, it is important to ensure image co-registration of tumors across multiple b-values or gradient directions. Otherwise, use of image co-registration software prior to DWI analysis is highly recommended to compensate for both rigid-body and non-rigid-body motions, especially for the liver and GI tract.

3.4 Influence of Contrast Agents on DWI Quantitative Measurements

Although DWI acquisitions are typically performed before administration of contrast agent, studies have shown that quantification of diffusion parameters does not exhibit significant difference before and after contrast agent administration (e.g., Gd-EOB-DTPA)[108,109]. This gives flexibility in adjusting the order of the pulse sequences in a protocol involving DWI. For example, the DWI can be performed during the enhancement delay after contrast injection to take advantage of the "dead time" and thus save the scan times.

3.5 ROI Selection for Quantitative Assessment

Selection of ROIs typically involves two steps. The first step is to determine the tumor-containing slice or slices, comprising single-slice (SS) selection, selection of three predefined slices (PD), observer-based (OB) volume[110], or whole tumor volume (WTV)[111]. The WTV method has the best repeatability and interobserver consistency, while the selective OB and SS methods can well approximate the WTV measurement and require significantly less measurement times, facilitating their adoption in a clinical setting[110,111].

The second step involves determination of ROI contours encasing all tumor areas within the chosen slice(s). The contour selection should reflect the specific study purpose. If the study is to investigate the biological aggressiveness, for example, the most restricted diffusion area should be selected by including a relatively small ROI in the highest DWI signal area. If the study is to investigate treatment response, the features of the whole tumor should be analyzed, and a contoured single-slice or WTV is recommended[96,112]. However, when encountering the situation of "node-in-mass" recurrent lesions, a small ROI can be more sensitive than using WTV in evaluating progressive disease (Figure 11). Furthermore, non-enhancing portions of lesion (e.g., hemorrhage or necrosis) should be excluded from the analysis as these areas can exhibit low ADC values, mimicking highly cellular portions of tumor.

3.6 Geometric Distortion

The majority of DWI studies are performed using single-shot EPI pulse sequences. As such, geometric distortion associated with EPI must be carefully considered. In diffusion-weighted EPI, image distortion arises from two primary sources: magnetic susceptibility and eddy

currents. The magnetic susceptibility can be particularly problematic for body imaging because of different tissue types. Distortion induced by magnetic susceptibility can be mitigated by using a high receiver bandwidth, parallel imaging, multi-shot sequences[113], etc. Eddy currents in diffusion-weighted EPI are produced primarily by the diffusion gradient. As the b-value increases, diffusion gradient becomes stronger and/or TE becomes longer, both of which exacerbate image distortion. Pulse sequences resilient to eddy currents, such as twice-refocused spin echo, can be used for high b-value DWI to reduce image distortion[114–116]. Various commercial software is also available to reduce the distortion after image acquisition.

4. Limitations and Possible Future Directions

Despite active research with growing number of publications on DWI with b-values spanning a wide range (i.e., 0–5000 s/mm^2), routine clinical use of DWI for cancer imaging is limited largely to qualitative assessment and quantification with ADC. Clinical adoption of many advanced high b-value DWI techniques with more sophisticated diffusion models is relatively slow. The low SNR, poor spatial resolution, and exacerbated image distortion at high b-values are among the technical impediments for clinical adoption. More importantly, the overlap in some quantitative diffusion parameters between benign and malignant lesions has limited their clinical utilization, despite the statistical differences observed in research studies. Because of these limitations, DWI must be interpreted in combination with conventional MR images and information from other advanced cancer imaging techniques[29,71].

Another factor contributing to the slow clinical adoption is lack of standardization and consensus, analogous to the Babel Tower effect[117]. Standardized image acquisition protocols, analysis procedures, and thresholds of quantitative parameters for diagnosis or treatment evaluation are indispensable for clinical applications. They will help establishing guidelines that can be used widely to improve impact. Unfortunately, among the vast amount of publications on DWI for cancer imaging, reports on consensus and standardization are scarce[4]. While each published study provides an excellent "building block", it is difficult to build a tower with blocks in different sizes and shapes.

Recent developments in two exciting areas may bring opportunities to resolve this dilemma and accelerate clinical translation of advanced DWI techniques. The first is radiomics with big data, which can potentially provide novel analysis tools of the existing data and lead to new insights into the best strategy for DWI standardization. This will greatly facilitate clinical trials to provide high evidence-based proofs of the values of advanced DWI for cancer care. The second is the multidisciplinary team (MDT) practice. This clinical practice model enhances the communication and understanding between radiologists, oncologists, and other clinicians not only during day-to-day patient care but also for conducting clinical trials. The oncologists' strong desire for more robust and sensitive imaging-based cancer biomarkers, coupled with radiologists' advanced quantitative DWI tools, will likely lead to fruitful efforts in standardization. Towards that end, the literature has already shown an encouraging progress on the validation of ADC as a cancer imaging marker in multicenter trials, through implementing standardized protocols across multivendor platforms together

with methods for quality assurance during the processes of data collection, archiving, curation, and analysis[118].

Conclusion

In conclusion, after more than three decades of development, DWI has become an important technique with widespread applications in many areas of cancer imaging, from diagnosis, tumor grading to treatment evaluation and prediction. Although the majority of current cancer applications rely on ADC, the rapid development of high b-value DWI techniques coupled with resurgence of the IVIM model has shown a strong trend to considerably expand the scope of DWI applications far beyond what ADC offers. At the present stage, reports of these advanced DWI techniques for cancer imaging are predominantly limited to individual findings. With further development in standardization of image acquisition and analysis, additional efforts in well-organized multi-center clinical trials, and enhanced interactions between radiologists and oncologists, DWI across the entire b-value spectrum is well positioned to become a powerful surrogate in cancer imaging to reveal sub-voxel tissue cellularity, vascularity, heterogeneity and microstructures that are important in cancer progression and regression.

Acknowledgements:

References

1. Le Bihan D, Breton E. Imagerie de diffusion in-vivo par résonance magnétique nucléaire. Comptes-Rendus l'Académie des Sci. 1985;93(5):27–34. https://hal.archives-ouvertes.fr/hal-00350090.

2. Moseley ME, Cohen Y, Mintorovitch J, et al. Early detection of regional cerebral ischemia in cats: Comparison of diffusion- and T2-weighted MRI and spectroscopy. Magn Reson Med. 1990;14(2):330–346. doi:10.1002/mrm.1910140218. [PubMed: 2345513]

3. Sorensen AG, Buonanno FS, Gonzalez RG, et al. Hyperacute stroke: evaluation with combined multisection diffusion-weighted and hemodynamically weighted echo-planar MR imaging. Radiology. 1996;199(2):391–401. doi:10.1148/radiology.199.2.8668784. [PubMed: 8668784]

4. Padhani AR, Liu G, Koh DM, et al. Diffusion-weighted magnetic resonance imaging as a cancer biomarker: consensus and recommendations. Neoplasia. 2009;11(2):102–125. http://www.ncbi.nlm.nih.gov/pubmed/19186405. [PubMed: 19186405]

5. De Santis S, Gabrielli A, Palombo M, Maraviglia B, Capuani S. Non-Gaussian diffusion imaging: A brief practical review. Magn Reson Imaging. 2011;29(10):1410–1416. doi:10.1016/j.mri.2011.04.006. [PubMed: 21601404]

6. McNab JA, Edlow BL, Witzel T, et al. The Human Connectome Project and beyond: Initial applications of 300mT/m gradients. Neuroimage. 2013;80:234–245. doi:10.1016/j.neuroimage. 2013.05.074. [PubMed: 23711537]

7. Chen L, Liu M, Bao J, et al. The Correlation between Apparent Diffusion Coefficient and Tumor Cellularity in Patients: A Meta-Analysis. PLoS One. 2013;8(11):e79008. doi:10.1371/journal.pone. 0079008. [PubMed: 24244402]

8. Jiang R, Ma Z, Dong H, Sun S, Zeng X, Li X. Diffusion tensor imaging of breast lesions: evaluation of apparent diffusion coefficient and fractional anisotropy and tissue cellularity. Br J Radiol. 2016;89(1064):20160076. doi:10.1259/bjr.20160076. [PubMed: 27302492]

9. Le Bihan D, Breton E, Lallemand D, Grenier P, Cabanis E, Laval-Jeantet M. MR imaging of intravoxel incoherent motions: application to diffusion and perfusion in neurologic disorders. Radiology. 1986;161(2):401–407. doi:10.1148/radiology.161.2.3763909. [PubMed: 3763909]

10. Iima M, Le Bihan D. Clinical Intravoxel Incoherent Motion and Diffusion MR Imaging: Past, Present, and Future. Radiology. 2016;278(1):13–32. doi:10.1148/radiol.2015150244. [PubMed: 26690990]

11. Koh D-M, Collins DJ, Orton MR. Intravoxel incoherent motion in body diffusion-weighted MRI: reality and challenges. AJR Am J Roentgenol. 2011;196(6):1351–1361. doi:10.2214/AJR.10.5515. [PubMed: 21606299]

12. Panagiotaki E, Chan RW, Dikaios N, et al. Microstructural Characterization of Normal and Malignant Human Prostate Tissue With Vascular, Extracellular, and Restricted Diffusion for Cytometry in Tumours Magnetic Resonance Imaging. Invest Radiol. 2015;50(4):218–227. doi: 10.1097/RLI.0000000000000115. [PubMed: 25426656]

13. Bickelhaupt S, Steudle F, Paech D, et al. On a fractional order calculus model in diffusion weighted breast imaging to differentiate between malignant and benign breast lesions detected on X-ray screening mammography. PLoS One. 2017;12(4):e0176077. doi:10.1371/journal.pone.0176077. [PubMed: 28453516]

14. Tang L, Sui Y, Zhong Z, et al. Non-Gaussian diffusion imaging with a fractional order calculus model to predict response of gastrointestinal stromal tumor to second-line sunitinib therapy. Magn Reson Med. 2018;79(3):1399–1406. doi:10.1002/mrm.26798. [PubMed: 28643387]

15. Clark CA, Le Bihan D. Water diffusion compartmentation and anisotropy at high b values in the human brain. Magn Reson Med. 2000;44(6):852–859. doi: 10.1002/1522-2594(200012)44:6<852::AID-MRM5>3.0.CO;2-A. [PubMed: 11108621]

16. Sehy JV, Banks A a, Ackerman JJH, Neil JJ. Importance of intracellular water apparent diffusion to the measurement of membrane permeability. Biophys J. 2002;83(5):2856–2863. doi:10.1016/S0006-3495(02)75294-6. [PubMed: 12414717]

17. Pilatus U, Shim H, Artemov D, Davis D, Van Zijl PCM, Glickson JD. Intracellular volume and apparent diffusion constants of perfused cancer cell cultures, as measured by NMR. Magn Reson Med. 1997;37(6):825–832. doi:10.1002/mrm.1910370605. [PubMed: 9178232]

18. Lai V, Li X, Lee VHF, Lam KO, Chan Q, Khong PL. Intravoxel incoherent motion MR imaging: Comparison of diffusion and perfusion characteristics between nasopharyngeal carcinoma and post-chemoradiation fibrosis. Eur Radiol. 2013;23(10):2793–2801. doi:10.1007/s00330-013-2889-8. [PubMed: 23722897]

19. Qi L-P, Yan W-P, Chen K-N, et al. Discrimination of Malignant versus Benign Mediastinal Lymph Nodes Using Diffusion MRI with an IVIM Model. Eur Radiol. 2018;28(3). doi:10.1007/s00330-017-5049-8.

20. Assaf Y, Blumenfeld-Katzir T, Yovel Y, Basser PJ. AxCaliber: a method for measuring axon diameter distribution from diffusion MRI. Magn Reson Med. 2008;59(6):1347–1354. doi:10.1002/mrm.21577. [PubMed: 18506799]

21. Zhang H, Schneider T, Wheeler-Kingshott CA, Alexander DC. NODDI: practical in vivo neurite orientation dispersion and density imaging of the human brain. Neuroimage. 2012;61(4):1000–1016. doi:10.1016/j.neuroimage.2012.03.072. [PubMed: 22484410]

22. Assaf Y, Basser PJ. Composite hindered and restricted model of diffusion (CHARMED) MR imaging of the human brain. Neuroimage. 2005;27(1):48–58. doi:10.1016/j.neuroimage. 2005.03.042. [PubMed: 15979342]

23. White NS, Leergaard TB, D'Arceuil H, Bjaalie JG, Dale AM. Probing tissue microstructure with restriction spectrum imaging: Histological and theoretical validation. Hum Brain Mapp. 2013;34(2):327–346. doi:10.1002/hbm.21454. [PubMed: 23169482]

24. Brunsing RL, Schenker-Ahmed NM, White NS, et al. Restriction spectrum imaging: An evolving imaging biomarker in prostate MRI. J Magn Reson Imaging. 2017;45(2):323–336. doi:10.1002/jmri.25419. [PubMed: 27527500]

25. Jensen JH, Helpern JA, Ramani A, Lu H, Kaczynski K. Diffusional kurtosis imaging: The quantification of non-Gaussian water diffusion by means of magnetic resonance imaging. Magn Reson Med. 2005;53:1432–1440. doi:10.1002/mrm.20508. [PubMed: 15906300]

26. Bennett KM, Schmainda KM, Bennett RT, Rowe DB, Lu H, Hyde JS. Characterization of continuously distributed cortical water diffusion rates with a stretched-exponential model. Magn Reson Med. 2003;50(4):727–734. doi:10.1002/mrm.10581. [PubMed: 14523958]

27. Zhou XJ, Gao Q, Abdullah O, Magin RL. Studies of anomalous diffusion in the human brain using fractional order calculus. Magn Reson Med. 2010;63(3):562–569. doi:10.1002/mrm.22285. [PubMed: 20187164]

28. Ingo C, Magin RLL, Colon-Perez L, Triplett W, Mareci THH. On random walks and entropy in diffusion-weighted magnetic resonance imaging studies of neural tissue. Magn Reson Med. 2014;71(2):617–627. doi:10.1002/mrm.24706. [PubMed: 23508765]

29. Karaman M, Sui Y, Wang H, et al. Differentiating Low- and High-Grade Pediatric Brain Using a Continuous-Time Random-Walk Diffusion Model at High b-Value. Magn Reson Med. 2016;76:1149–1157. doi:10.1002/mrm.26012. [PubMed: 26519663]

30. Fan Y, Gao J-H. Fractional motion model for characterization of anomalous diffusion from NMR signals. Phys Rev E. 2015;92(1):12707. doi:10.1103/PhysRevE.92.012707.

31. Karaman M, Wang H, Sui Y, Engelhard H, Li Y, Zhou XJ. A Fractional Motion Diffusion Model for Grading Pediatric Brain Tumors. NeuroImage Clin. 2016;12:707–714. [PubMed: 27761401]

32. Tamura C, Shinmoto H, Soga S, et al. Diffusion kurtosis imaging study of prostate cancer: Preliminary findings. J Magn Reson Imaging. 2014;40(3):723–729. doi:10.1002/jmri.24379. [PubMed: 24924835]

33. Zhu L, Pan Z, Ma Q, et al. Diffusion Kurtosis Imaging Study of Rectal Adenocarcinoma Associated with Histopathologic Prognostic Factors: Preliminary Findings. Radiology. 2017;284(1):66–76. doi:10.1148/radiol.2016160094. [PubMed: 27929929]

34. Bai Y, Lin Y, Tian J, et al. Grading of Gliomas by Using Monoexponential, Biexponential, and Stretched Exponential Diffusion-weighted MR Imaging and Diffusion Kurtosis MR Imaging. Radiology. 2016;278(2):496–504. doi:10.1148/radiol.2015142173. [PubMed: 26230975]

35. Magin RL, Abdullah O, Baleanu D, Zhou XJ. Anomalous diffusion expressed through fractional order differential operators in the Bloch-Torrey equation. J Magn Reson. 2008;190(2):255–270. doi:10.1016/j.jmr.2007.11.007. [PubMed: 18065249]

36. Reynaud O Time-Dependent Diffusion MRI in Cancer: Tissue Modeling and Applications. Front Phys. 2017;5:58. doi:10.3389/fphy.2017.00058.

37. Park MJ, Kim YK, Choi S, Rhim H, Lee WJ, Choi D. Preoperative Detection of Small Pancreatic Carcinoma: Value of Adding Diffusion-weighted Imaging to Conventional MR Imaging for Improving Confidence Level. Radiology. 2014;273(2):433–443. doi:10.1148/radiol.14132563. [PubMed: 24991989]

38. Tang L, Sun Y-S, Li Z-Y, et al. Diffusion-weighted magnetic resonance imaging in the depiction of gastric cancer: initial experience. Abdom Radiol. 2016;41(1):2–9. doi:10.1007/s00261-015-0594-6.

39. Wang L, Lin J, Liu K, et al. Intravoxel incoherent motion diffusion-weighted MR imaging in differentiation of lung cancer from obstructive lung consolidation: comparison and correlation with pharmacokinetic analysis from dynamic contrast-enhanced MR imaging. Eur Radiol. 2014;24(8):1914–1922. doi:10.1007/s00330-014-3176-z. [PubMed: 24788038]

40. Ichikawa T, Erturk SM, Motosugi U, et al. High-B-Value Diffusion-Weighted MRI in Colorectal Cancer. Am J Roentgenol. 2006;187(1):181–184. doi:10.2214/AJR.05.1005. [PubMed: 16794174]

41. Kim CK, Park BK, Kim B. High-b-Value Diffusion-Weighted Imaging at 3 T to Detect Prostate Cancer: Comparisons Between b Values of 1,000 and 2,000 s/mm ^{2}. Am J Roentgenol. 2010;194(1):W33–W37. doi:10.2214/AJR.09.3004. [PubMed: 20028888]

42. Wetter A, Nensa F, Lipponer C, et al. High and ultra-high b-value diffusion-weighted imaging in prostate cancer: a quantitative analysis. Acta radiol. 2015;56(8):1009–1015. doi: 10.1177/0284185114547900. [PubMed: 25168023]

43. Rockall AG. Diffusion weighted MRI in ovarian cancer. Curr Opin Oncol. 2014;26(5):529–535. doi:10.1097/CCO.0000000000000112. [PubMed: 25024053]

44. Kele PG, van der Jagt EJ. Diffusion weighted imaging in the liver. World J Gastroenterol. 2010;16(13):1567–1576. doi:10.3748/WJG.V16.I13.1567. [PubMed: 20355235]

45. Godley KC, Syer TJ, Toms AP, et al. Accuracy of high b-value diffusion-weighted MRI for prostate cancer detection: a meta-analysis. Acta radiol. 2018;59(1):105–113. doi: 10.1177/0284185117702181. [PubMed: 28376634]

46. Woo S, Suh CH, Kim SY, Cho JY, Kim SH. Head-To-Head Comparison Between High- and Standard-b-Value DWI for Detecting Prostate Cancer: A Systematic Review and Meta-Analysis. Am J Roentgenol. 2018;210(1):91–100. doi:10.2214/AJR.17.18480. [PubMed: 28952806]

47. Purysko AS, Rosenkrantz AB, Barentsz JO, Weinreb JC, Macura KJ. PI-RADS Version 2: A Pictorial Update. RadioGraphics. 2016;36(5):1354–1372. doi:10.1148/rg.2016150234. [PubMed: 27471952]

48. DeLano MC, Cooper TG, Siebert JE, Potchen MJ, Kuppusamy K. High-b-value diffusion-weighted MR imaging of adult brain: image contrast and apparent diffusion coefficient map features. AJNR. 21(10):1830–1836. http://www.ncbi.nlm.nih.gov/pubmed/11110534. Accessed March 20, 2018.

49. Mazaheri Y, Afaq A, Rowe DB, Lu Y, Shukla-Dave A, Grover J. Diffusion-weighted magnetic resonance imaging of the prostate: improved robustness with stretched exponential modeling. J Comput Assist Tomogr. 2012;36(6):695–703. doi:10.1097/RCT.0b013e31826bdbbd. [PubMed: 23192207]

50. Liu X, Zhou L, Peng W, Wang H, Zhang Y. Comparison of stretched-Exponential and monoexponential model diffusion-Weighted imaging in prostate cancer and normal tissues. J Magn Reson Imaging. 2015;42(4):1078–1085. doi:10.1002/jmri.24872. [PubMed: 25727776]

51. Ertas G, Onaygil C, Akin Y, Kaya H, Aribal E. Quantitative differentiation of breast lesions at 3T diffusion-weighted imaging (DWI) using the ratio of distributed diffusion coefficient (DDC). J Magn Reson Imaging. 2016;44(6):1633–1641. doi:10.1002/jmri.25327. [PubMed: 27284961]

52. Demetri GD, Reichardt P, Kang Y-K, et al. Efficacy and safety of regorafenib for advanced gastrointestinal stromal tumours after failure of imatinib and sunitinib (GRID): an international, multicentre, randomised, placebo-controlled, phase 3 trial. Lancet. 2013;381(9863):295–302. doi: 10.1016/S0140-6736(12)61857-1. [PubMed: 23177515]

53. Dijkstra H, Dorrius MD, Wielema M, et al. Semi-automated quantitative intravoxel incoherent motion analysis and its implementation in breast diffusion-weighted imaging. J Magn Reson Imaging. 2016;43(5):1122–1131. doi:10.1002/jmri.25086. [PubMed: 26558851]

54. Nishie A, Kakihara D, Asayama Y, et al. Apparent diffusion coefficient: An associative factor for recurrence after nephrectomy in localized renal cell carcinoma. J Magn Reson Imaging. 2016;43(1):166–172. doi:10.1002/jmri.24984. [PubMed: 26082268]

55. Woodhams R, Kakita S, Hata H, et al. Identification of Residual Breast Carcinoma Following Neoadjuvant Chemotherapy: Diffusion-weighted Imaging—Comparison with Contrast-enhanced MR Imaging and Pathologic Findings. Radiology. 2010;254(2):357–366. doi:10.1148/radiol. 2542090405. [PubMed: 20093508]

56. Bradley WG, Golding SG, Herold CJ, et al. Globalization of P4 Medicine: Predictive, Personalized, Preemptive, and Participatory—Summary of the Proceedings of the Eighth International Symposium of the International Society for Strategic Studies in Radiology, August 27–29, 2009. Radiology. 2011;258(2):571–582. doi:10.1148/radiol.10100568. [PubMed: 21273521]

57. Louis DN, Perry A, Reifenberger G, et al. The 2016 World Health Organization Classification of Tumors of the Central Nervous System: a summary. Acta Neuropathol. 2016;131(6):1–18. doi: 10.1007/s00401-016-1545-1. [PubMed: 26715564]

58. Allred DC, Wu Y, Mao S, et al. Ductal carcinoma in situ and the emergence of diversity during breast cancer evolution. Clin Cancer Res. 2008;14(2):370–378. doi: 10.1158/1078-0432.CCR-07-1127. [PubMed: 18223211]

59. Humphrey PA. Gleason grading and prognostic factors in carcinoma of the prostate. Mod Pathol. 2004;17(3):292–306. doi:10.1038/modpathol.3800054. [PubMed: 14976540]

60. Maley CC, Galipeau PC, Finley JC, et al. Genetic clonal diversity predicts progression to esophageal adenocarcinoma. Nat Genet. 2006;38(4):468–473. doi:10.1038/ng1768. [PubMed: 16565718]

61. Kwee TC, Galbán CJ, Tsien C, et al. Intravoxel water diffusion heterogeneity imaging of human high-grade gliomas. NMR Biomed. 2010;23(2):179–187. doi:10.1002/nbm.1441. [PubMed: 19777501]

62. Sui Y, Wang H, G L, et al. Differentiation of Low- and High-Grade Pediatric Brain Tumors with High b-Value Diffusion-weighted MR Imaging and a Fractional Order Calculus Model. Radiology. 2015;277(2):489–496. [PubMed: 26035586]

63. Sui Y, Xiong Y, Jiang J, Zhu W, Zhou XJ. Differentiab of Low- and High-Grade Gliomas Using High b-Value Diffusion Imaging with A non-Gaussian Diffusion Model. Am J Neuroradiol. 2016;37(9):1643–1649. [PubMed: 27256851]

64. Liu GZ, Xie KL, Sui Y, et al. Diffusion-Weighted MR Imaging of Prostate with A Fractional Order Calculus Model. In: The 21st Annual Meeting of the International Society for Magnetic Resonance in Medicine; 2013:1783.

65. Szczepankiewicz F, van Westen D, Englund E, et al. The link between diffusion MRI and tumor heterogeneity: Mapping cell eccentricity and density by diffusional variance decomposition (DIVIDE). Neuroimage. 2016;142:522–532. doi:10.1016/J.NEUROIMAGE.2016.07.038. [PubMed: 27450666]

66. Wen Q, Kelley DAC, Banerjee S, et al. Clinically feasible NODDI characterization of glioma using multiband EPI at 7 T. NeuroImage Clin. 2015;9:291–299. doi:10.1016/J.NICL.2015.08.017. [PubMed: 26509116]

67. Wang F, Wang Y, Zhou Y, et al. Comparison between types I and II epithelial ovarian cancer using histogram analysis of monoexponential, biexponential, and stretched-exponential diffusion models. J Magn Reson Imaging. 2017;46(6):1797–1809. doi:10.1002/jmri.25722. [PubMed: 28379611]

68. Roethke MC, Kuder TA, Kuru TH, et al. Evaluation of Diffusion Kurtosis Imaging Versus Standard Diffusion Imaging for Detection and Grading of Peripheral Zone Prostate Cancer. Invest Radiol. 2015;50(8):483–489. doi:10.1097/RLI.0000000000000155. [PubMed: 25867657]

69. Chatterjee A, Bourne RM, Wang S, et al. Diagnosis of Prostate Cancer with Noninvasive Estimation of Prostate Tissue Composition by Using Hybrid Multidimensional MR Imaging: A Feasibility Study. *Radiology*. 2018;287(3):864–873. doi:10.1148/radiol.2018171130. [PubMed: 29393821]

70. Kang TW, Kim SH, Jang KM, et al. Gastrointestinal stromal tumours: Correlation of modified NIH risk stratification with diffusion-weighted MR imaging as an imaging biomarker. Eur J Radiol. 2015;84(1):33–40. doi:10.1016/j.ejrad.2014.10.020. [PubMed: 25466773]

71. Lee J, Kim SH, Kang TW, Song KD, Choi D, Jang KT. Mass-forming Intrahepatic Cholangiocarcinoma: Diffusion-weighted Imaging as a Preoperative Prognostic Marker. Radiology. 2016;281(1):119–128. doi:10.1148/radiol.2016151781. [PubMed: 27115053]

72. Nasu K, Kuroki Y, Minami M. Diffusion-weighted imaging findings of mucinous carcinoma arising in the ano-rectal region: comparison of apparent diffusion coefficient with that of tubular adenocarcinoma. Jpn J Radiol. 2012;30(2):120–127. doi:10.1007/s11604-011-0023-x. [PubMed: 22173559]

73. Stevanović S, Pasetto A, Helman SR, et al. Landscape of immunogenic tumor antigens in successful immunotherapy of virally induced epithelial cancer. Science. 2017;356(6334):200–205. doi:10.1126/science.aak9510. [PubMed: 28408606]

74. Choueiri TK, Escudier B, Powles T, et al. Cabozantinib versus Everolimus in Advanced Renal-Cell Carcinoma. N Engl J Med. 2015;373(19):1814–1823. doi:10.1056/NEJMoa1510016. [PubMed: 26406150]

75. Levy A, Hollebecque A, Ferté C, et al. Tumor Assessment Criteria in Phase I Trials: Beyond RECIST. J Clin Oncol. 2013;31(3):395–395. doi:10.1200/JCO.2012.46.2184. [PubMed: 23248247]

76. Wen PY, Macdonald DR, Reardon DA, et al. Updated Response Assessment Criteria for High-Grade Gliomas: Response Assessment in Neuro-Oncology Working Group. J Clin Oncol. 2010;28(11):1963–1972. doi:10.1200/JCO.2009.26.3541. [PubMed: 20231676]

77. Tang L, Zhang X-P, Sun Y-S, et al. Gastrointestinal Stromal Tumors Treated with Imatinib Mesylate: Apparent Diffusion Coefficient in the Evaluation of Therapy Response in Patients. Radiology. 2011;258(3):729–738. doi:10.1148/radiol.10100402. [PubMed: 21193597]

78. Liang H-Y, Huang Y-Q, Yang Z-X, Ying-Ding, Zeng M-S, Rao S-X. Potential of MR histogram analyses for prediction of response to chemotherapy in patients with colorectal hepatic metastases. Eur Radiol. 2016;26(7):2009–2018. doi:10.1007/s00330-015-4043-2. [PubMed: 26494642]

79. Szurowska E, Nowicki TK, Izycka-Swieszewska E, Zadrozny D, Markiet K, Studniarek M. Predictive value of apparent diffusion coefficient in evaluation of colorectal carcinoma hepatic metastases' response to radiofrequency ablation. J Magn Reson Imaging. 2013;38(5):1027–1032. doi:10.1002/jmri.24089. [PubMed: 23526807]

80. Qu J, Qin L, Cheng S, et al. Residual low ADC and high FA at the resection margin correlate with poor chemoradiation response and overall survival in high-grade glioma patients. Eur J Radiol. 2016;85(3):657–664. doi:10.1016/j.ejrad.2015.12.026. [PubMed: 26860681]

81. Jung SH, Heo SH, Kim JW, et al. Predicting response to neoadjuvant chemoradiation therapy in locally advanced rectal cancer: Diffusion-weighted 3 tesla MR imaging. J Magn Reson Imaging. 2012;35(1):110–116. doi:10.1002/jmri.22749. [PubMed: 21989997]

82. Mannelli L, Kim S, Hajdu CH, Babb JS, Taouli B. Serial diffusion-weighted MRI in patients with hepatocellular carcinoma: Prediction and assessment of response to transarterial chemoembolization. Preliminary experience. Eur J Radiol. 2013;82(4):577–582. doi:10.1016/j.ejrad.2012.11.026. [PubMed: 23246330]

83. Cho GY, Gennaro L, Sutton EJ, et al. Intravoxel incoherent motion (IVIM) histogram biomarkers for prediction of neoadjuvant treatment response in breast cancer patients. Eur J Radiol Open. 2017;4:101–107. doi:10.1016/j.ejro.2017.07.002. [PubMed: 28856177]

84. Moffat B a, Chenevert TL, Lawrence TS, et al. Functional diffusion map: a noninvasive MRI biomarker for early stratification of clinical brain tumor response. Proc Natl Acad Sci U S A. 2005;102(15):5524–5529. doi:10.1073/pnas.0501532102. [PubMed: 15805192]

85. Mardor Y, Pfeffer R, Spiegelmann R, et al. Early detection of response to radiation therapy in patients with brain malignancies using conventional and high b-value diffusion-weighted magnetic resonance imaging. J Clin Oncol. 2003;21(6):1094–1100. doi:10.1200/JCO.2003.05.069. [PubMed: 12637476]

86. Chen X, Ma Z, Huang Y, et al. Multiparametric MR diffusion-weighted imaging for monitoring the ultra-early treatment effect of sorafenib in human hepatocellular carcinoma xenografts. J Magn Reson Imaging. 2017;46(1):248–256. doi:10.1002/jmri.25527. [PubMed: 27783444]

87. Mardor Y, Roth Y, Ocherashvili A, et al. Pretreatment Prediction of Brain Tumors Response to Radiation Therapy Using High b-Value Diffusion-Weighted MRI. Neoplasia. 2004;6(2):136–142. doi:10.1593/neo.03349. [PubMed: 15140402]

88. McDonald CR, Delfanti RL, Krishnan AP, et al. Restriction spectrum imaging predicts response to bevacizumab in patients with high-grade glioma. Neuro Oncol. 2016;18(11):now063. doi:10.1093/neuonc/now063.

89. Zhu H-B, Zhang X-Y, Zhou X-H, et al. Assessment of pathological complete response to preoperative chemoradiotherapy by means of multiple mathematical models of diffusion-weighted MRI in locally advanced rectal cancer: A prospective single-center study. J Magn Reson Imaging. 2017;46(1). doi:10.1002/jmri.25567.

90. Vroomen LGPH, Scheffer HJ, Melenhorst MCAM, et al. MR and CT imaging characteristics and ablation zone volumetry of locally advanced pancreatic cancer treated with irreversible electroporation. Eur Radiol. 2017;27(6):2521–2531. doi:10.1007/s00330-016-4581-2. [PubMed: 27659702]

91. Shintani T, Matsuo Y, Iizuka Y, et al. Assessment of treatment response after lung stereotactic body radiotherapy using diffusion weighted magnetic resonance imaging and positron emission tomography: A pilot study. Eur J Radiol. 2017;92:58–63. doi:10.1016/j.ejrad.2017.04.022. [PubMed: 28624021]

92. Kokabi N, Camacho JC, Xing M, Edalat F, Mittal PK, Kim HS. Immediate post-doxorubicin drug-eluting beads chemoembolization Mr Apparent diffusion coefficient quantification predicts response in unresectable hepatocellular carcinoma: A pilot study. J Magn Reson Imaging. 2015;42(4):981–989. doi:10.1002/jmri.24845. [PubMed: 25683022]

93. Rieger J, Bähr O, Müller K, Franz K, Steinbach J, Hattingen E. Bevacizumab-induced diffusion-restricted lesions in malignant glioma patients. J Neurooncol. 2010;99(1):49–56. doi:10.1007/s11060-009-0098-8. [PubMed: 20035366]

94. Quaia E, Gennari AG, Ricciardi MC, Ulcigrai V, Angileri R, Cova MA. Value of percent change in tumoral volume measured at T_2-weighted and diffusion-weighted MRI to identify responders after neoadjuvant chemoradiation therapy in patients with locally advanced rectal carcinoma. J Magn Reson Imaging. 2016;44(6):1415–1424. doi:10.1002/jmri.25310. [PubMed: 27219471]

95. Giganti F, De Cobelli F, Canevari C, et al. Response to chemotherapy in gastric adenocarcinoma with diffusion-weighted MRI and ^{18} F-FDG-PET/CT: Correlation of apparent diffusion coefficient and partial volume corrected standardized uptake value with histological tumor regression grade. J Magn Reson Imaging. 2014;40(5):1147–1157. doi:10.1002/jmri.24464. [PubMed: 24214734]

96. Xu Q, Xu Y, Sun H, et al. Quantitative intravoxel incoherent motion parameters derived from whole-tumor volume for assessing pathological complete response to neoadjuvant chemotherapy in locally advanced rectal cancer. J Magn Reson Imaging. 12 2017. doi:10.1002/jmri.25931.

97. Schraml C, Schwenzer NF, Martirosian P, et al. Diffusion-Weighted MRI of Advanced Hepatocellular Carcinoma During Sorafenib Treatment: Initial Results. Am J Roentgenol. 2009;193(4):W301–W307. doi:10.2214/AJR.08.2289. [PubMed: 19770299]

98. Shi C, Liu D, Xiao Z, et al. Monitoring Tumor Response to Antivascular Therapy Using Non-Contrast Intravoxel Incoherent Motion Diffusion-Weighted MRI. Cancer Res. 2017;77(13):3491–3501. doi:10.1158/0008-5472.CAN-16-2499. [PubMed: 28487383]

99. Jiang J, Yin J, Cui L, et al. Lung Cancer: Short-Term Reproducibility of Intravoxel Incoherent Motion Parameters and Apparent Diffusion Coefficient at 3T. J Magn Reson Imaging. 2018;47(4):1003–1012. doi:10.1002/jmri.25820. [PubMed: 28741732]

100. Kakite S, Dyvorne H, Besa C, et al. Hepatocellular carcinoma: short-term reproducibility of apparent diffusion coefficient and intravoxel incoherent motion parameters at 3.0T. J Magn Reson Imaging. 2015;41(1):149–156. doi:10.1002/jmri.24538. [PubMed: 24415565]

101. Winfield JM, deSouza NM, Priest AN, et al. Modelling DW-MRI data from primary and metastatic ovarian tumours. Eur Radiol. 2015;25(7):2033–2040. doi:10.1007/s00330-014-3573-3. [PubMed: 25605133]

102. Jerome NP, Miyazaki K, Collins DJ, et al. Repeatability of derived parameters from histograms following non-Gaussian diffusion modelling of diffusion-weighted imaging in a paediatric oncological cohort. Eur Radiol. 2017;27(1):345–353. doi:10.1007/s00330-016-4318-2. [PubMed: 27003140]

103. Chen X, Qin L, Pan D, et al. Liver Diffusion-weighted MR Imaging: Reproducibility Comparison of ADC Measurements Obtained with Multiple Breath-hold, Free-breathing, Respiratory-triggered, and Navigator-triggered Techniques. Radiology. 2014;271(1):113–125. doi:10.1148/radiol.13131572. [PubMed: 24475860]

104. Bernardin L, Douglas NHM, Collins DJ, et al. Diffusion-weighted magnetic resonance imaging for assessment of lung lesions: repeatability of the apparent diffusion coefficient measurement. Eur Radiol. 2014;24(2):502–511. doi:10.1007/s00330-013-3048-y. [PubMed: 24275802]

105. Weller A, Papoutsaki MV, Waterton JC, et al. Diffusion-weighted (DW) MRI in lung cancers: ADC test-retest repeatability. Eur Radiol. 2017;27(11):4552–4562. doi:10.1007/s00330-017-4828-6. [PubMed: 28396997]

106. Kim SY, Lee SS, Park B, et al. Reproducibility of measurement of apparent diffusion coefficients of malignant hepatic tumors: effect of DWI techniques and calculation methods. J Magn Reson Imaging. 2012;36(5):1131–1138. doi:10.1002/jmri.23744. [PubMed: 22777895]

107. Lee Y, Lee SS, Kim N, et al. Intravoxel incoherent motion diffusion-weighted MR imaging of the liver: effect of triggering methods on regional variability and measurement repeatability of quantitative parameters. Radiology. 2015;274(2):405–415. doi:10.1148/radiol.14140759. [PubMed: 25232802]

108. Colagrande S, Mazzoni LN, Mazzoni E, Pradella S. Effects of gadoxetic acid on quantitative diffusion-weighted imaging of the liver. J Magn Reson Imaging. 2013;38(2):365–370. doi: 10.1002/jmri.23978. [PubMed: 23239165]

109. Dorrius MD, Dijkstra H, Oudkerk M, Sijens PE. Effect of b value and pre-admission of contrast on diagnostic accuracy of 1.5-T breast DWI: a systematic review and meta-analysis. Eur Radiol. 2014;24(11):2835–2847. doi:10.1007/s00330-014-3338-z. [PubMed: 25103535]

110. Ahlawat S, Khandheria P, Del Grande F, et al. Interobserver variability of selective region-of-interest measurement protocols for quantitative diffusion weighted imaging in soft tissue masses: Comparison with whole tumor volume measurements. J Magn Reson Imaging. 2016;43(2):446–454. doi:10.1002/jmri.24994. [PubMed: 26174705]

111. Priola AM, Priola SM, Gned D, et al. Diffusion-weighted quantitative MRI of pleural abnormalities: Intra- and interobserver variability in the apparent diffusion coefficient measurements. J Magn Reson Imaging. 2017;46(3):769–782. doi:10.1002/jmri.25633. [PubMed: 28117923]

112. Blazic IM, Lilic GB, Gajic MM. Quantitative Assessment of Rectal Cancer Response to Neoadjuvant Combined Chemotherapy and Radiation Therapy: Comparison of Three Methods of Positioning Region of Interest for ADC Measurements at Diffusion-weighted MR Imaging. Radiology. 2017;282(2):418–428. doi:10.1148/radiol.2016151908. [PubMed: 27253423]

113. Bernstein MA, King KF, Zhou XJ. Handbook of MRI Pulse Sequences.; 2004. doi:10.1016/B978-0-12-092861-3.X5000-6.

114. Reese TG, Heid O, Weisskoff RM, Wedeen VJ. Reduction of eddy-current-induced distortion in diffusion MRI using a twice-refocused spin echo. Magn Reson Med. 2003;49(1):177–182. [PubMed: 12509835]

115. Gao Q, Srinivasan G, Magin RL, Zhou XJ. Anomalous diffusion measured by a twice-refocused spin echo pulse sequence: analysis using fractional order calculus. J Magn Reson Imaging. 2011;33(5):1177–1183. doi:10.1002/jmri.22522. [PubMed: 21509877]

116. Karaman MM, Zhou XJ. A fractional motion diffusion model for a twice-refocused spin echo pulse sequence. NMR Biomed. 2018;(in press).

117. Guiu B, Cercueil J-P. Liver diffusion-weighted MR imaging: the tower of Babel? Eur Radiol. 2011;21(3):463–467. doi:10.1007/s00330-010-2017-y. [PubMed: 21110195]

118. deSouza NM, Winfield JM, Waterton JC, et al. Implementing diffusion-weighted MRI for body imaging in prospective multicentre trials: current considerations and future perspectives. Eur Radiol. 2018;28(3):1118–1131. doi:10.1007/s00330-017-4972-z. [PubMed: 28956113]
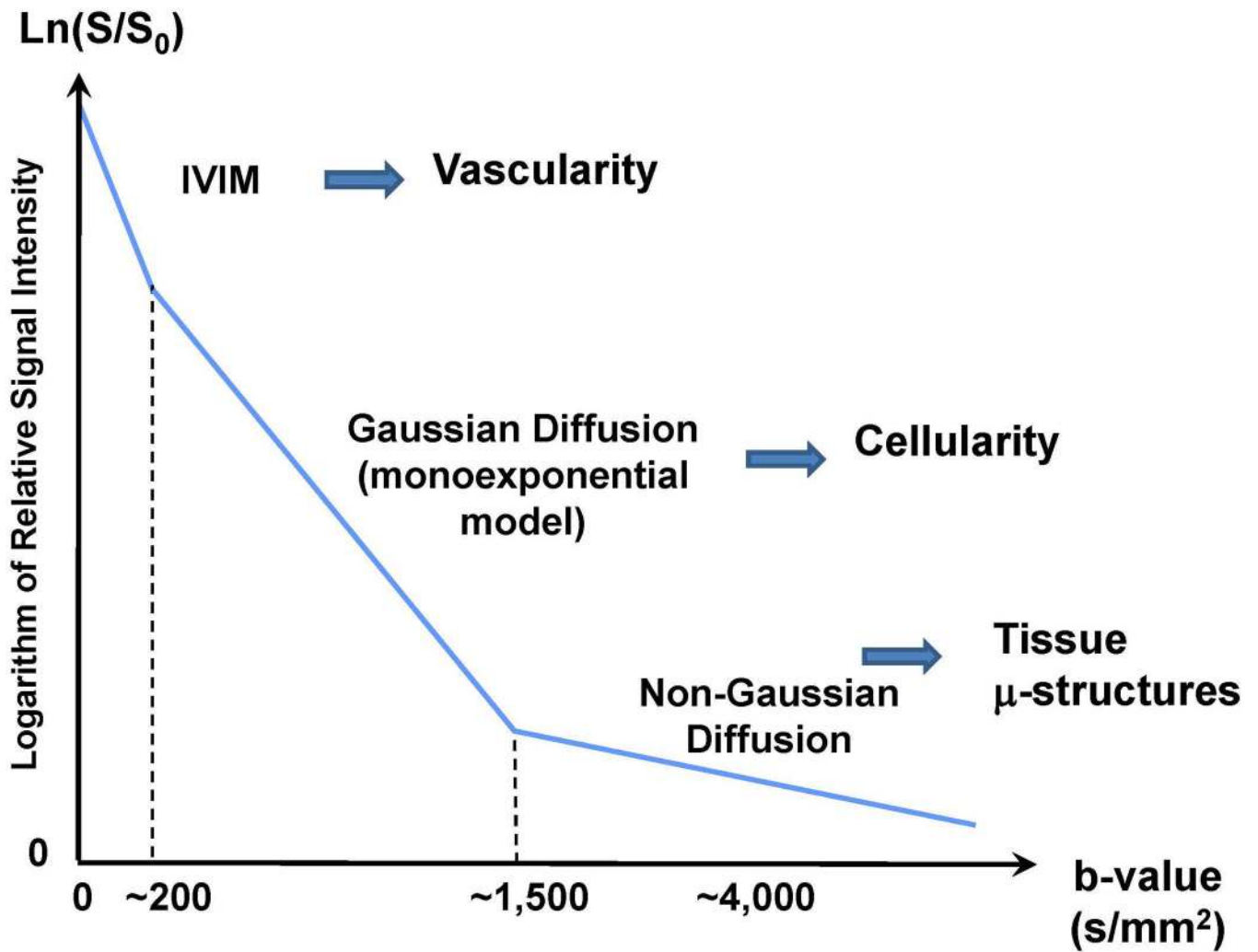
Figure 1.
Diffusion-induced signal attenuation as a function of b-value. Three regions are highlighted in the plot with low, intermediate, and high b-values, respectively, each corresponding to a specific tissue property that can be probed by DWI. The b-values on the horizontal axis are illustrating examples and can be varied depending on the applications.
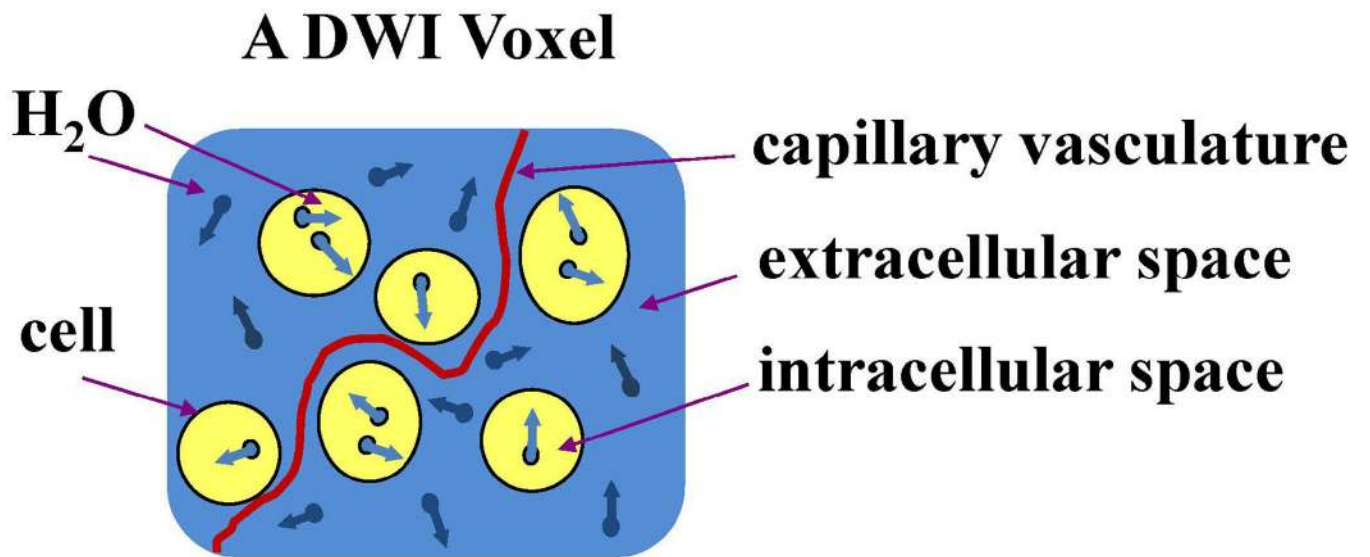
Figure 2.
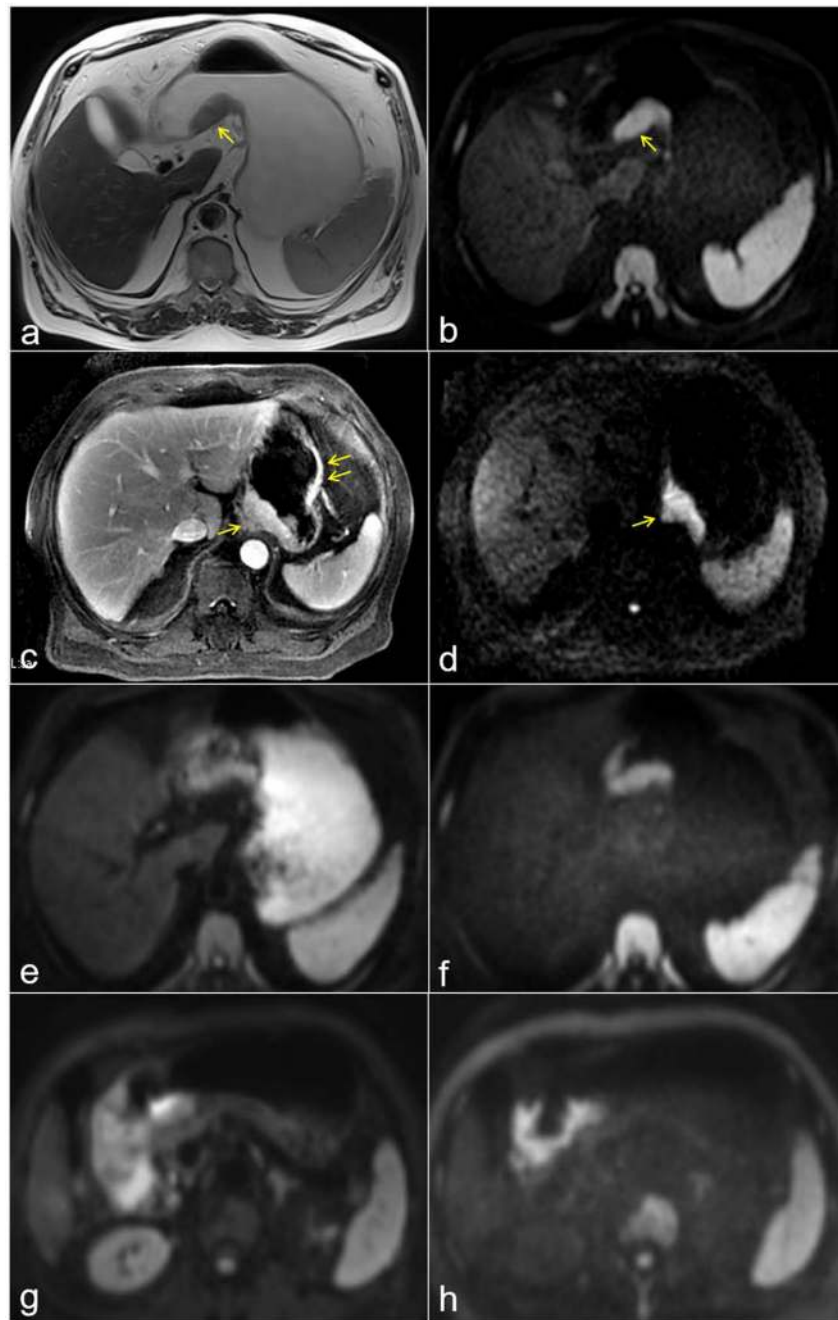An image voxel in DWI, containing intra- and extra-cellular spaces and capillary vasculature
as annotated.

Figure 3.
Examples of using DWI for tumor detection. Images in each row were acquired from the same patient. (a)-(b): On a patient with gastric cancer in antrum (arrow), the contrast between the lesion (arrow) and the background tissue was much higher on the DWI with b=1000 s/mm^2 (b) than on the T2W image (a). (c)-(d): T1 enhancement was observed on a patient with esophagogastric junction cancer (arrow; (c)). However, the opposite larger curvature wall also displayed strong enhancement (double arrow), making it difficult to determine the tumor border. On the DWI with b=1000 s/mm^2 (d), the normal wall signal was effectively suppressed, making the cancer easily detectable (arrow). (e)-(h): On a patient

with gastric cancer in antrum, the conspicuity of the tumor improved substantially when the b-value was increased from 300 s/mm^2 in (e) to 1200 s/mm^2 in (f). Similar improvement was observed on another patient when the b-value was increased from 500 s/mm^2 in (g) to 1200 s/mm^2 in (h).
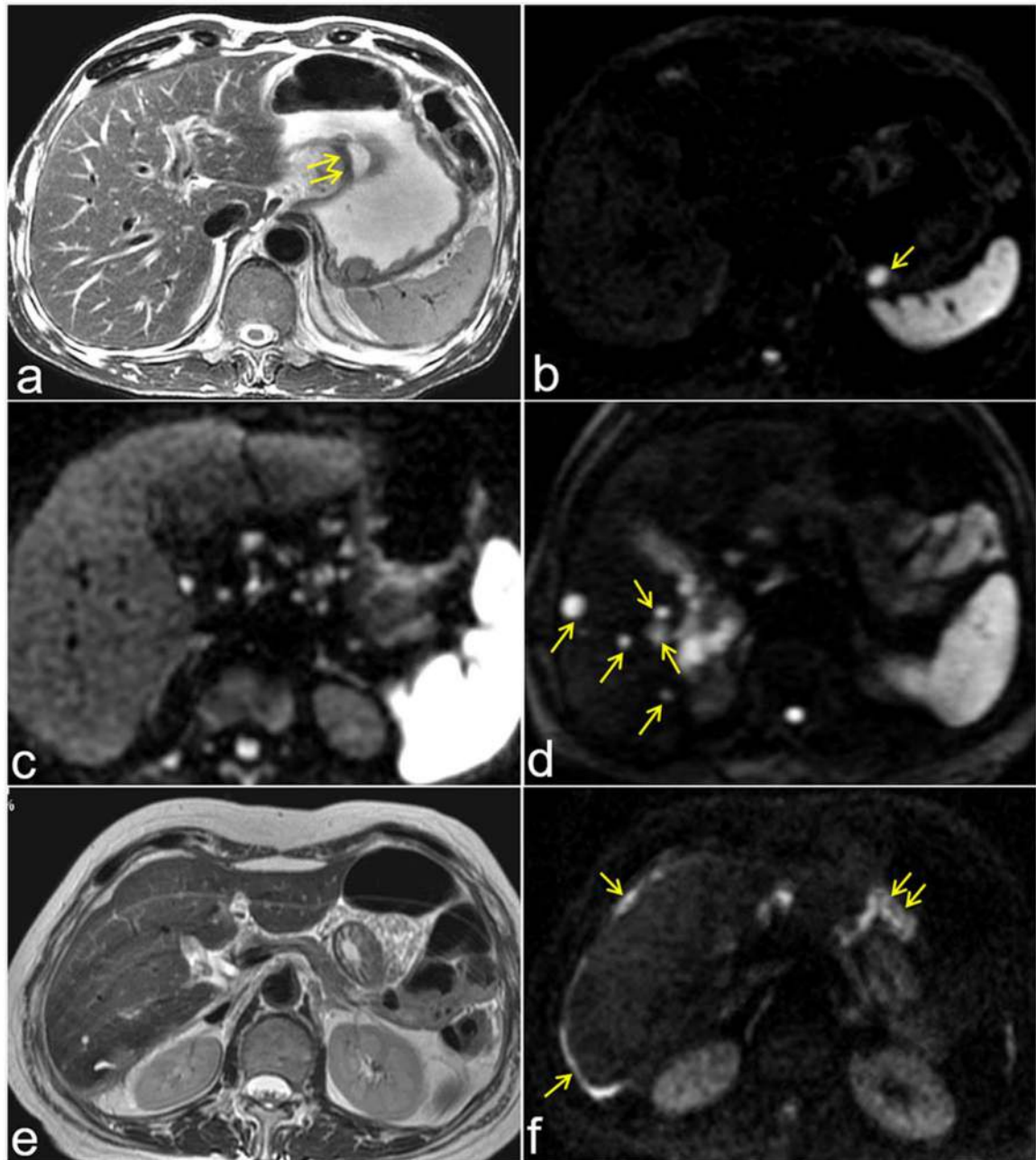
Figure 4.
Examples of using DWI to detect small tumors that are not easily visible in convention MRI. (a)-(b): A gastric malignancy in lesser curvature (double arrow) was seen in the T2W image (arrow in (a)). Using DWI with b=1000s/mm^2, an additional small lesion (arrow in (b)) was detected and proven as a GIST by operational pathology. (c)-(d): DWI was effective in highlighting small metastatic lesions in the small lymph nodes (c) and in the liver (d). (e)-(f): In this patient with gastric cancer, no definite sign of metastasis on the T2W image was observed (e). However, diffuse dissemination in perihepatic peritoneum (arrow) and omentum (double arrows) were clearly seen on DWI with b=1000s/mm^2 (f).
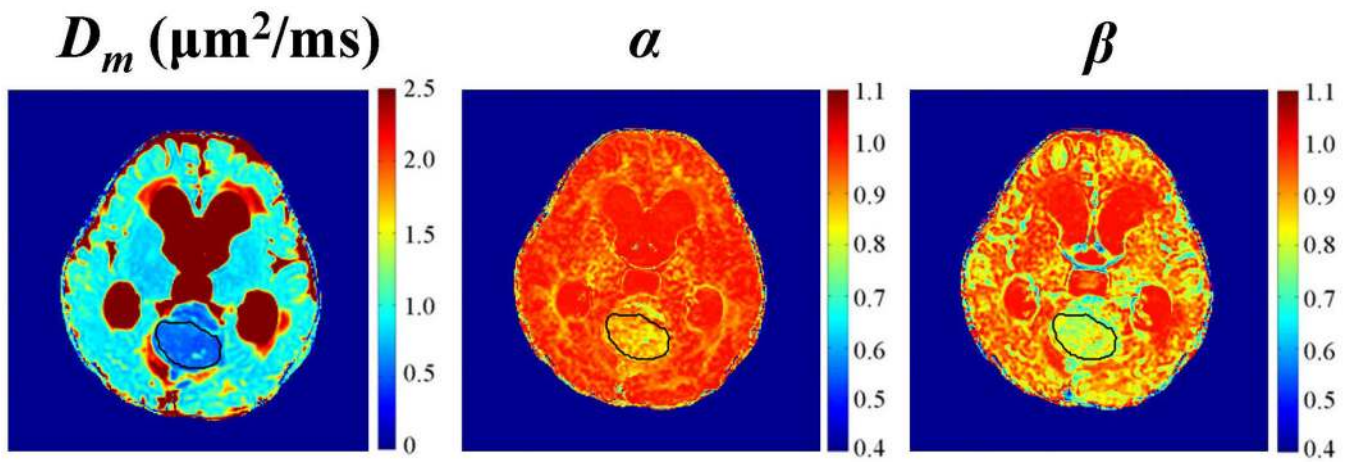
Figure 5.
Maps of *D*, *α* and *β* from a CTRW model demonstrating good contrasts between a medulloblastoma and its surrounding normal brain tissue from an 18-month old girl. These parameter maps should be used conjointly with conventional images based on T1, T2 and FLAIR contrasts to improve tumor detection and characterization.
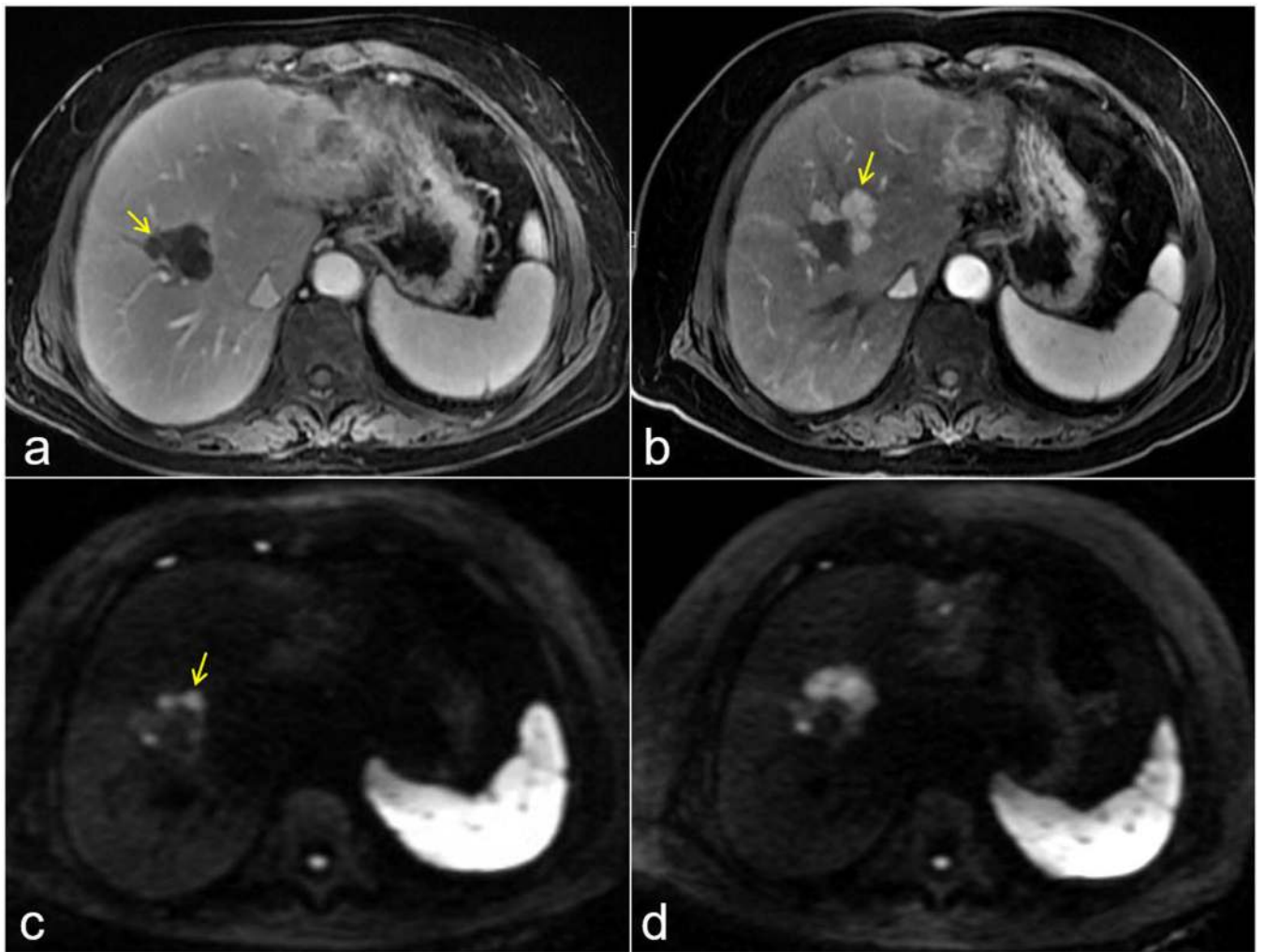
Figure 6.
Contrast-enhanced T1W images (top row) and diffusion-weighted images (bottom row) of an HCC patient who received RFA treatment. No obvious enhancement was seen near the post-RFA area (arrow in (a)). However, small recurrent lesions were detected in DWI (arrow in (b)) with much improved contrast. These lesions were confirmed in both contrast-enhanced T1W (c) and diffusion-weighted images (d) at one-month follow-up.
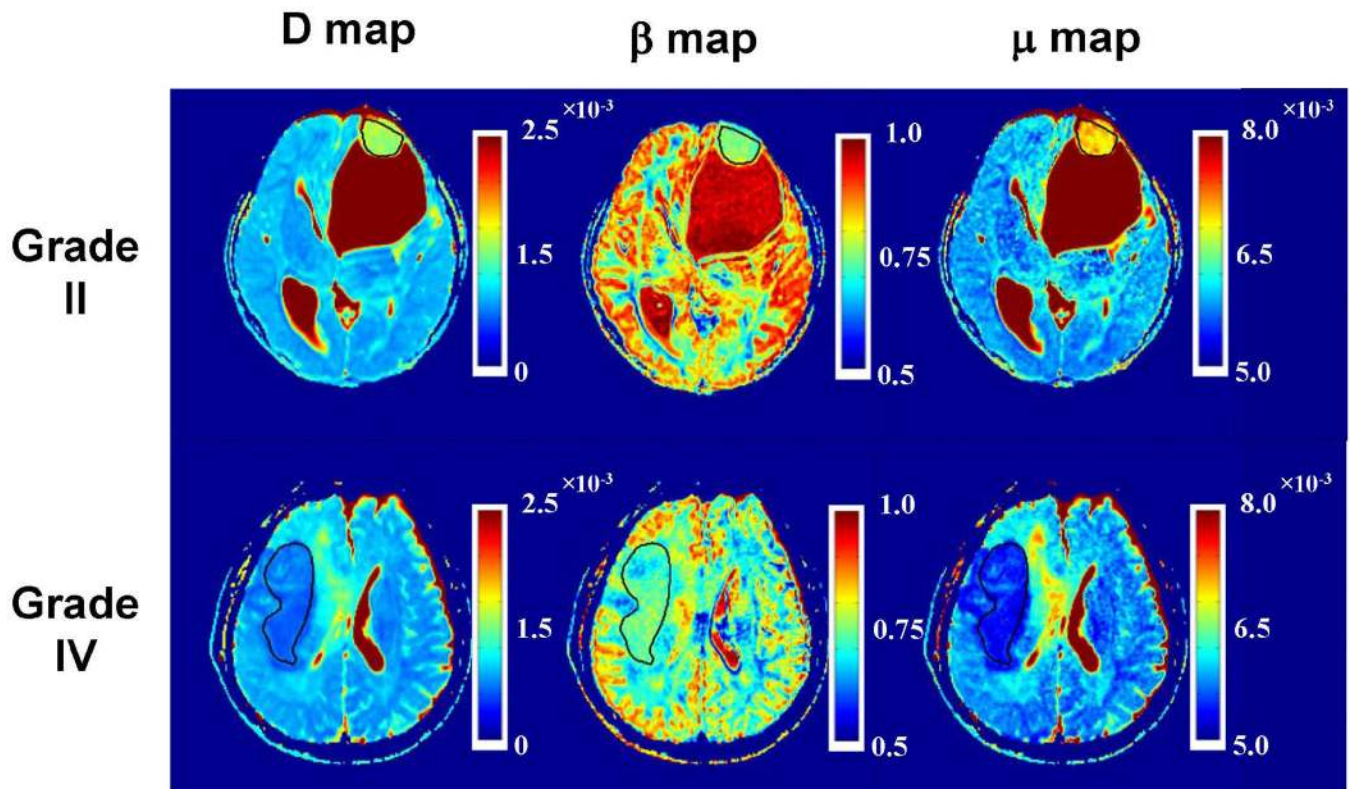
Figure 7.

FROC maps of a grade II glioma patient (upper row) and a grade IV glioblastoma patient (lower row). D, β, and μ are the FROC parameters defined in Eqs. [6] and [7] with their physical meanings explained in the text. In particular, β has been related to intra-voxel tissue heterogeneity. Differences between the two tumors can be seen in each of the three maps.
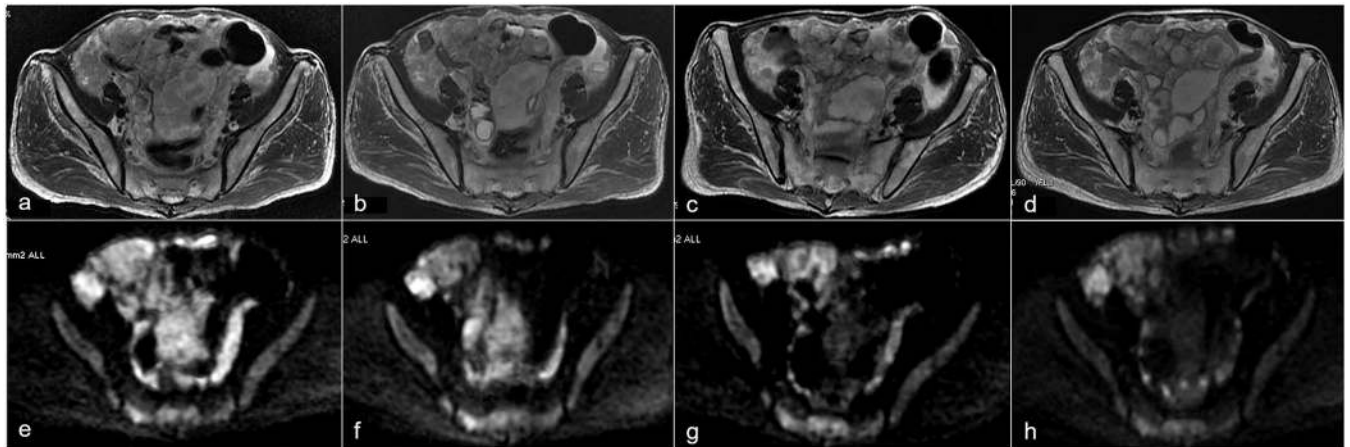
Figure 8.
Demonstration of DWI for quantitatively monitoring early change of GIST following imatinib targeted therapy in a patient with diffusely metastasis lesions in the abdomen. T2W and diffusion-weighted images are shown in the top and bottom row, respectively. Each column represents a time point: (a) and (e): pre-treatment; (b) and (f): three days; (c) and (g): one week; and (d) and (h): four weeks after initiation of the treatment. T2W images showed fused irregular tumors without appreciable change in tumor size until a later time point (d). In addition, the tumor size was difficult to measure because of the irregular shape. In contrast, the mean ADC exhibited a substantial increase only after 3 days of treatment (1.09×10^{-3} mm^2/s in (e) versus 1.34×10^{-3} mm^2/s in (f)). The mean ADC continued to increase for weeks during the treatment (1.83×10^{-3} mm^2/s in (g) after one week and 1.96×10^{-3} mm^2/s in (h) after four weeks).
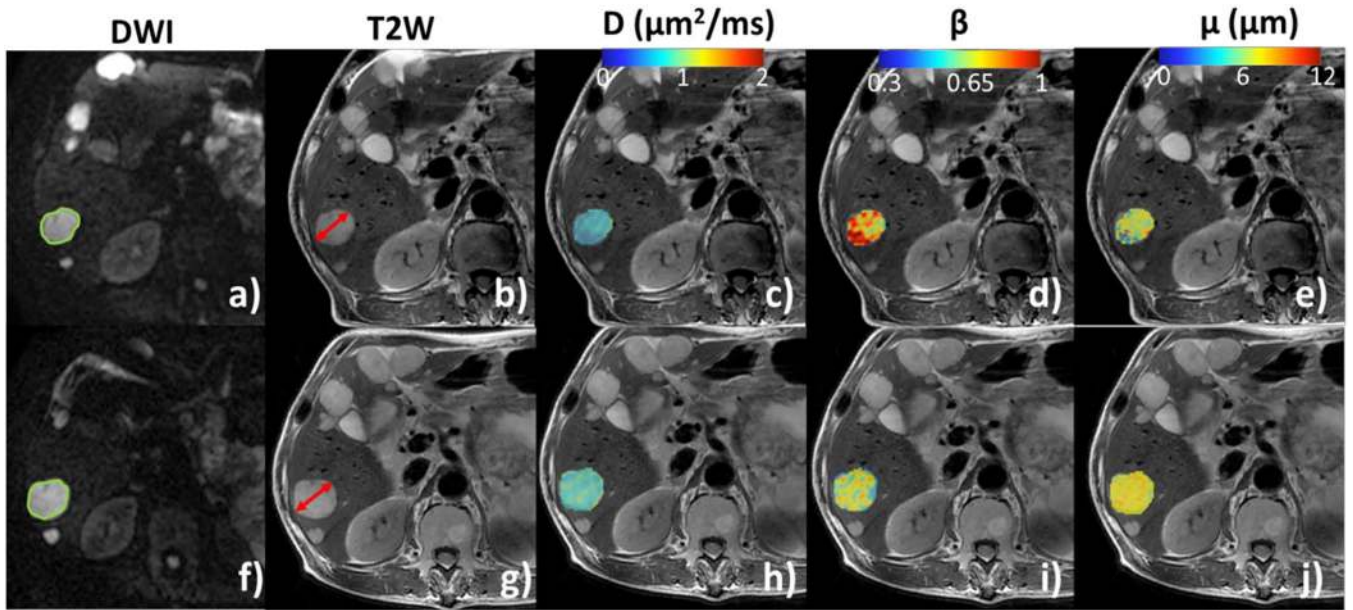
Figure 9.
Demonstration of FROC parameters for monitoring early changes of a GIST patient following sunitinib targeted therapy. Images of pre-treatment baseline and two weeks after initiation of treatment are displayed in the top and bottom row, respectively. The first two columns correspond to ADC ((a) and (f)) and T2W images ((b) and (g)). The remaining three columns show the D, β and μ color maps of a lesion superimposed on the T2W image, respectively. The color bars in these three columns display the quantitative scales for the respective parameter (D in units of $\times 10^{-3}$ mm^2/s, β between 0 and 1, and μ in units of μm). The tumor size measured from the T2W images ((b) vs. (g)) did not change. ADC ((a) vs. (f)) and D ((c) vs. (h)) showed minimal change. However, β decreased substantially ((d) vs. (i)), and μ increased moderately ((e) vs. (j)) two weeks after the initiation of sunitinib targeted therapy. The results may signify potentially good response of tumors to sunitinib, which may confirm the treatment decision more quickly.
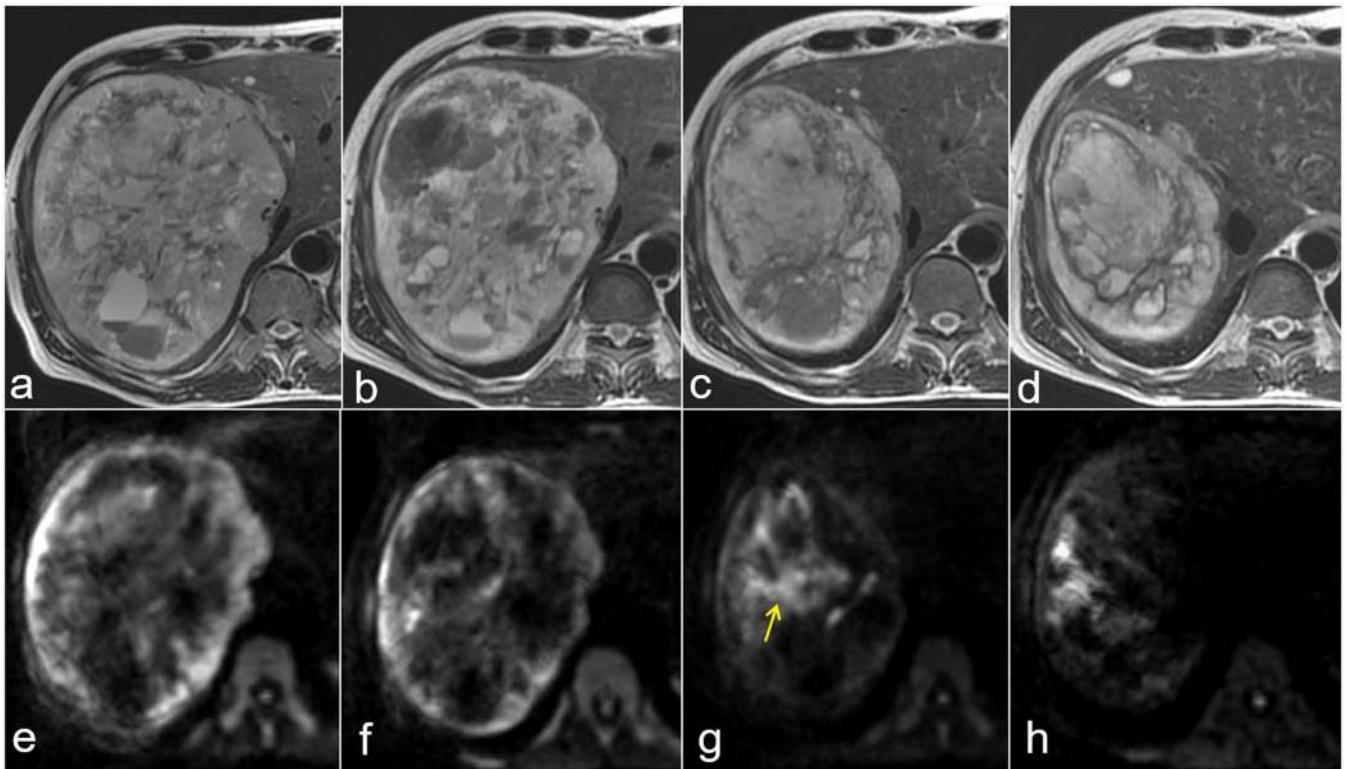
Figure 10.
Demonstration of confounding pathologic changes during targeted therapy of liver metastasis. T2W and diffusion-weighted images are shown in the top and bottom row, respectively. Each column represents a time point: (a) and (e): pre-treatment; (b) and (f): one week; (c) and (g): one month; and (d) and (h): three months after initiation of treatment. Prior to treatment, a large tumor on the right liver lobe was clearly visible with mixed signals ((a) and (e)). One week after the treatment, no appreciable tumor size change was observed in the T2W image (b). The DWI showed decreased signal (f) with the corresponding increase in ADC (not shown). At the one-month time point, the tumor size decreased (c). However, hypersignal appeared on DWI in the center of tumor (arrow in (g)), which *may* signify progression. At the three-month time point, however, the tumor size continued to shrink (d), suggesting that the hypersignals in (g) and (h) were most likely inner degeneration or abscess that mimics recurrence, instead of recurrence.
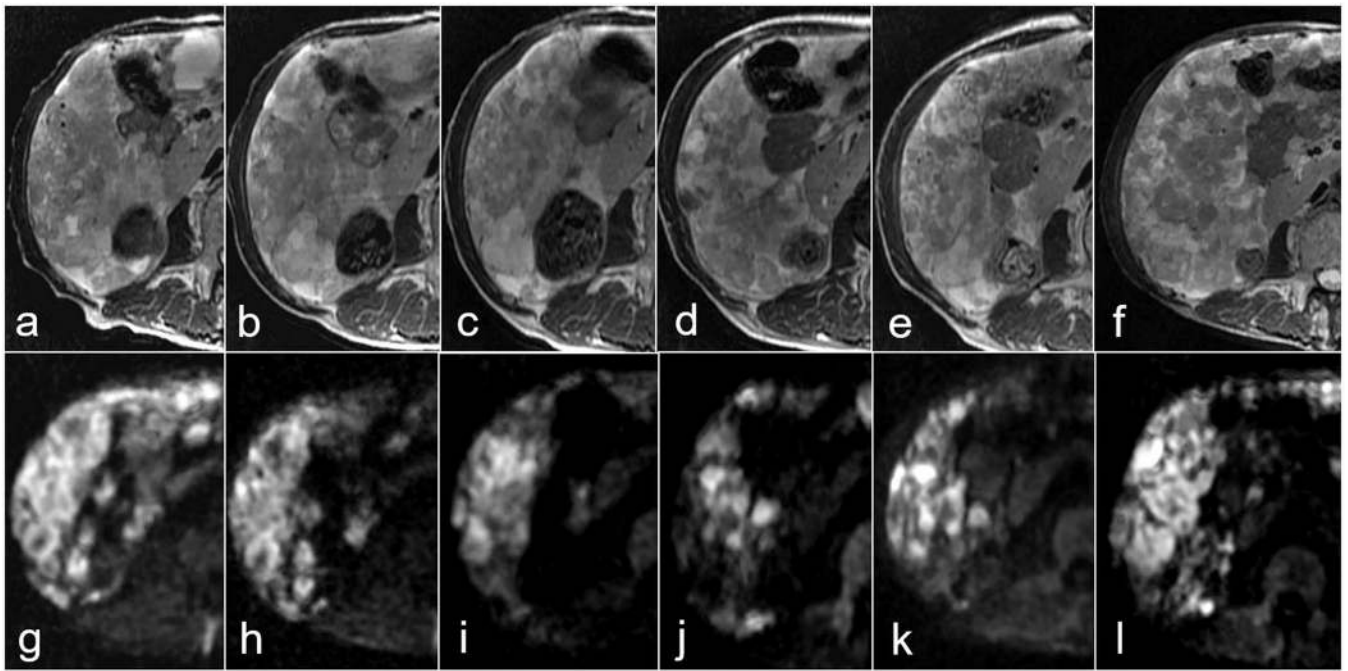
Figure 11.
A case of diffuse metastasis tumors to demonstrate that a small ROI can be more sensitive than WTV to detecting progressive disease. T2W and diffusion-weighted images are shown in the top and bottom row, respectively. From left to right, each column represents a time point: pre-treatment baseline, three days, one week, two weeks, four weeks, and three months after treatment, sequentially. Throughout the time course, both the mean ADC (ADC_{mean}) and minimum ADC (ADC_{min}) were measured from the tumors. The values of ADC_{mean} were 0.91×10^{-3} (g), 1.19×10^{-3} (h), 1.39×10^{-3} (i), 1.72×10^{-3} (j), 1.38×10^{-3} (k), and 0.96×10^{-3} mm^2/s (l), whereas the values of ADC_{min} were 0.77×10^{-3} (g), 0.94×10^{-3} (h), 1.02×10^{-3} (i), 0.91×10^{-3} (j), 0.85×10^{-3} (k), and 0.95×10^{-3} mm^2/s (l). A quantitative analysis showed that ADC_{min} was more sensitive than ADC_{mean} during the tumor response and recurrent processes, concurrent with the increase and decrease in ADC, respectively. This illustrates the benefit of using a small ROI to focus on high DWI signal regions in this specific example.

Table 1.

Summary of Selected Diffusion Models for Cancer Imaging

	Model	Parameters	b-Value range * (s/mm^2)	Typical number of b-values	Biological significance of the parameters
	mono-exponential	ADC	0–1000	2	cellularity
compartmentalized non-Gaussian models	IVIM	D, D^*, f	0–200; 600–1000	3–12	cellularity, vascularity
	bi-exponential	D_f, D_s, f	0–3000	≥4	cellularity, volume fraction, cell membrane
	NODDI	$\nu_{iso}, \nu_{in}, \nu_{exv}$ ODI, plus DTI parameters	0, ~700–1000; ~2000–3000	3	microstructures, neurite dispersion orientation and density
	AxCaliber	f_h, f_r plus q-space imaging parameters	0–4000 **	multi-shell q-space acquisition **	microstructures, fiber diameter distribution, hindered and restricted structures
	RSI	component fractions f_i	0–1000 (for prostate)	≥4; multi-shell q-space acquisition	microstructures, hindered and restricted structures, cellularity map
	VERDICT	volume fractions: f_{IC}, f_{EES}, f_{VASC}, R_{cell} diffusion or pseudo diffusion coefficients	0–3000	~9	microstructures, cell radius index, volume fractions of intracellular, extracellular-extravascular, and vascular spaces
non-compartmentalized non-Gaussian models	stretched exponential	DDC, α	0–4000	≥3	cellularity distribution, heterogeneity
	DKI	D, K	0–4000	≥3	general microstructures
	FROC	D, β, μ	0–4000	~5–12	cellularity, intra-voxel heterogeneity, microscopic scale
	CTRW	D, α, β	0–4000	~6–18	cellularity, intra-voxel heterogeneities, microenvironment
	fractional motion	D, φ, ψ	0–4000	~6–18	microstructures as measured by diffusion variance and correlation

*
The b-value range is for typical clinical applications on commercial scanners.

**
This is a q-space imaging technique that requires varying both diffusion gradient and diffusion time.